LUND UNIVERSITY

Simulation and prediction of pulmonary flow in patients with Fontan circulation

Frieberg, Petter

2023

Document Version:
Publisher's PDF, also known as Version of record

[Link to publication](#)

Total number of authors:
1

LUND UNIVERSITY

PO Box 117
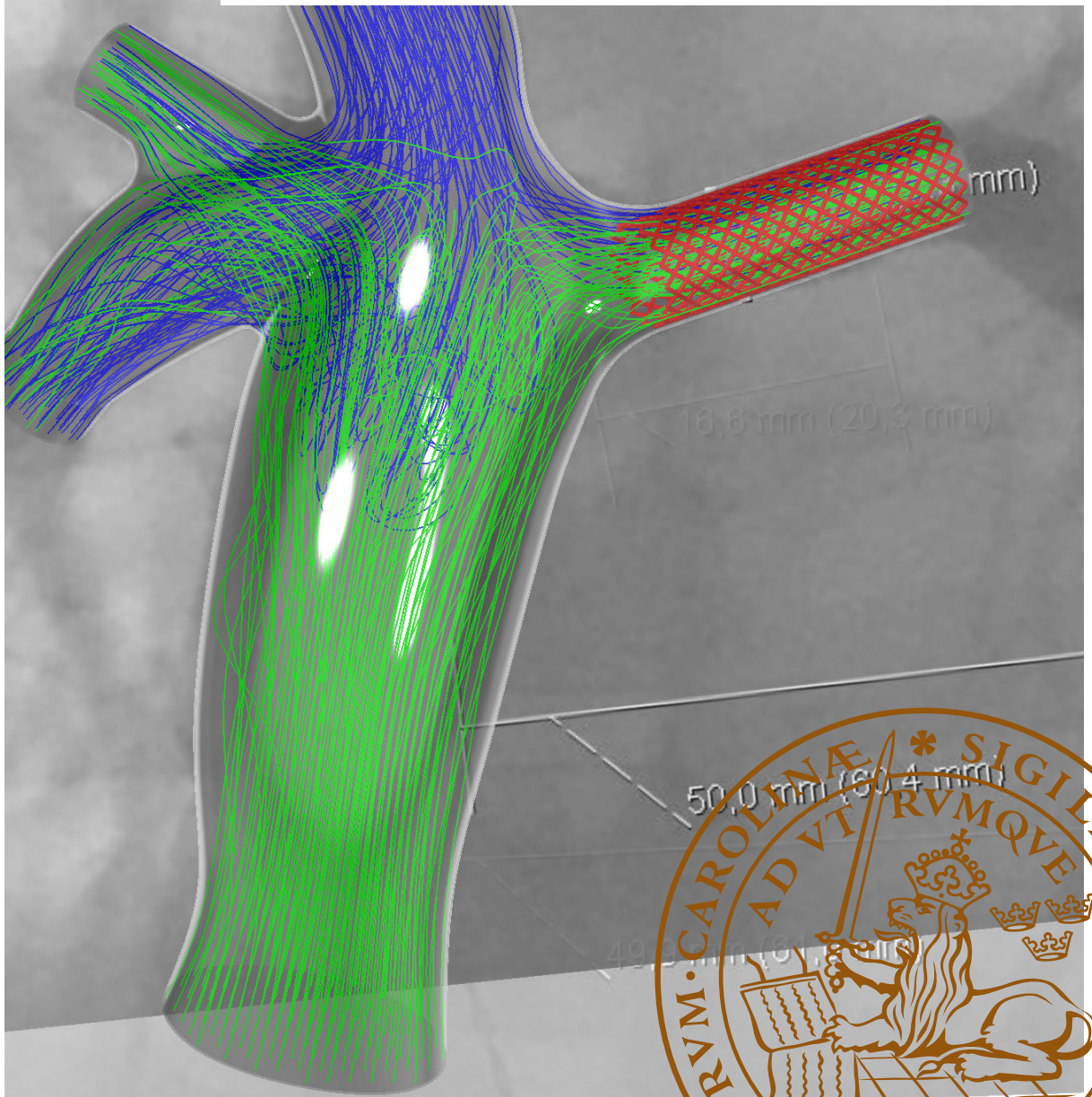221 00 Lund
+46 46-222 00 00

Simulation and prediction of pulmonary flow in patients with Fontan circulation

PETTER FRIEBERG

DEPARTMENT OF CLINICAL PHYSIOLOGY | FACULTY OF MEDICINE | LUND UNIVERSITY

Simulation and prediction of pulmonary flow in patients
with Fontan circulation

Simulation and prediction of pulmonary flow in patients with Fontan circulation

Petter Frieberg

Organization: LUND UNIVERSITY, Skåne University Hospital, Clinical Sciences, Department of Clinical Physiology, Entrégatan 7, SE 22242 Lund

Document name: Doctoral dissertation	**Date of issue**
Author(s): Petter Frieberg	**Sponsoring organization:**

Title and subtitle: Simulation and prediction of pulmonary flow in patients with Fontan circulation

Abstract:

Approximately 1% of children are born with congenital heart disease. Some patients may require surgery with staged conversion to a circulation with a univentricular heart, known as a Fontan circulation. The heart then only pumps to the aorta, and deoxygenated venous blood flows passively to the lungs via surgical connections of the caval veins directly to the pulmonary arteries. Pulmonary flow is however hard to predict and additional invasive interventions may be required as the child grows older, which is burdensome for the patient and the health care system. Therefore, this thesis aimed to provide a framework for predictive computer simulations of pulmonary flow based on data obtained from non-invasive magnetic resonance imaging (MRI).

Study I described how MRI data can be used to create three-dimensional models for use with computational fluid dynamics (CFD) to simulate pulmonary flow. The study also demonstrated two cases where the method could be used to predict pulmonary flow after invasive interventions.

Study II validated our method with a more complex and established CFD method, and with patient-specific flows measured in MRI. Our metod obtained the same results as the advanced method in just five minutes compared with 10-12 hours. Both methods agreed with MRI measurements.

Study III showed how blood flow from the liver to the lungs relates to pulmonary resistance, pulmonary blood flow and oxygen saturation at rest. A patient case showed how CFD was used to help design an invasive intervention, where results in terms of pulmonary flow and saturation agreed with predictions.

Study IV was a prospective study where predictive simulations on the day before the final stage in univentricular heart surgery were compared with MRI results obtained approximately six months after surgery. Results showed good agreement in terms of the amount of total- and liver blood to the lungs.

In summary, this thesis showed that simulations can predict pulmonary flow in patients with Fontan circulation and that such simulations can be performed within a day of an MRI examination.

Key words: Fontan circulation, computational fluid dynamics, endovascular intervention, surgical planning, vascular physiology

Classification system and/or index terms (if any)	Supplementary bibliographical information
Language: English	**ISSN and key title**: 1652-8220

Lund University, Faculty of Medicine Doctoral Dissertation Series 2023:36

ISBN: 978-91-8021-375-2

Recipient's notes	**Number of pages**:
Price	Security classification

Signature	Date 2023-02-16

Simulation and prediction of pulmonary flow in patients with Fontan circulation

Petter Frieberg, M.D.

Faculty opponent

Professor Sir Shakeel Qureshi, Evelina London Children's Hospital

Evaluation Committee

Professor Birgitta Janerot Sjöberg, Karolinska Institutet

Associate professor Jonas Lantz, Linköping University

Professor Sandra Lindstedt, Lund University

When you have exhausted all possibilities, remember this:
You haven't.

Thomas Edison

Table of Contents

List of publications

Paper I

Simulation of aortopulmonary collateral flow in Fontan patients for use in prediction of interventional outcomes

Frieberg P, Sjöberg P, Revstedt J, Heiberg E, Liuba P, Carlsson M. Clin Physiol Funct Imaging. 2018;38(4).

Paper II

Computational Fluid Dynamics Support for Fontan Planning in Minutes, Not Hours: The Next Step in Clinical Pre-Interventional Simulations

Frieberg, P., Aristokleous, N., Sjöberg, P., Töger J., Liuba P., Carlsson M. J. of Cardiovasc. Trans. Res. 2021 Dec.

Paper III

In vivo hepatic flow distribution by computational fluid dynamics can predict pulmonary flow distribution in Fontan patients

Frieberg, P., Sjöberg, P., Hedström, E., Carlsson, M., Liuba, P. Manuscript.

Paper IV

Time-effective computational predictions of pulmonary flow in patients after Fontan completion

Frieberg, P., Sjöberg, P., Tran P-K., Liuba, P., Carlsson, M. Manuscript.

All publications are reproduced with the permission of their respective publishers.

Author's contribution to the publications

	Study design	Ethical application	Data collection	Data analysis	Statistics	Figures and tables	Interpretation of results	Preparation of manuscript	Revision of manuscript	Response to reviewers
Paper I	2	0	0	3	3	3	3	3	3	3
Paper II	3	2	2	3	3	3	3	2	3	3
Paper III	3	2	3	3	3	3	3	3	-	-
Paper IV	2	3	3	3	3	3	3	3	-	-

Not applicable	-
No contribution	0
Limited contribution	1
Moderate contribution	2
Significant contribution	3

Abbreviations

APC	Aorto-pulmonary collaterals
AVSD	Atrio-ventricular septum defect
CFD	Computational fluid dynamics
DILV	Double inlet left ventricle
DORV	Double outlet right ventricle
HLHS	Hypoplastic left heart syndrome
HRHS	Hypoplastic right heart syndrome
IVC	Inferior vena cava
LA	Left atrium
LPA	Left pulmonary artery
LPV	Left pulmonary vein
LV	Left ventricle
MRI	Magnetic resonance imaging
PA	Pulmonary atresia
PVR	Pulmonary vascular resistance
RA	Right atrium
RPA	Right pulmonary artery
RPV	Right pulmonary vein
RV	Right ventricle
SCV	Superior vena cava
TCPC	Total cavo-pulmonary connection
TGA	Transposition of the great arteries
VSD	Ventricle septum defect
VVC	Veno-venous collaterals

Acknowledgements

While I cannot thank everyone individually or as much as I'd like for their help and support in making this thesis come true, there are some to whom I'd specifically would like to extend my gratitude:

To my main supervisor **Marcus Carlsson** for your amazing ability to be present, for your patience with me when I'm confused, for challenging me, and for helping me to improve myself along the way.

To my co-supervisor **Petru Liuba** for your incredible energy, humbleness, and kindness. I can really think of no-one who embodies this better than you. To my co-supervisors **Johan Revstedt** for being there and always helping me when I most need it, and to **Johannes Töger** for your calm and reasoning ways and for challenging me with problems that have really sharpened my CFD skills.

To professor **Håkan Arheden** for your care and passion to help us and find the way towards self-realization, individually and as a team.

To the steering committee, PhD students and all colleagues in the **Lund Cardiac MR group**: the workplace you represent is incredible and absolutely unique. I deeply appreciate every day, every meeting and every passing conversation in the corridors and offices.

To all colleagues at the clinic of **Clinical Physiology and Nuclear medicine** and to head of department **Jonas Jögi**: your care for the workplace, for the patients, and for each other is inspiring. I so often hear from patients how pleased they are with the work you achieve.

To all colleagues and PhD students at the **Paediatric Heart Center**: Thank you for your comradeship and for including me in your workplace, with special appreciations to **Kiet Tran** and **Jens Johansson-Ramgren** for inviting me to attend surgeries that leave me in awe of your skill and craftmanship. To **Zahraa Alsafi** and **Elin Friberg** for all your hard work in recruiting patients, the fun we have together and how much I look forward to every time we meet.

To **Einar Heiberg** and everyone at Medviso for your fantastic entrepreneur spirit and positive attitude. To **Katarina Steding-Ehrenborg** for all goofy conversations on astronauts, space, life on earth and stuff in between. To **Pia Sjöberg** for your support, great ideas and kindness.

To **Jonas Liefke** for your generosity and for providing a smile in every situation. It rubs off. To **Anders Nelsson** for always being a good friend. To **Ann-Helen Arvidsson** for your helpfulness, amazing can-do spirit and constructive thinking.

To my wife **Mimmi Anderberg** for being my best friend and for all the groovy things we do. Your humour, generosity and incredible creativity is such an inspiration to me.

To my brother and sister **Klas Maharadja Frieberg** and **Nilla Käck** for always supporting me and checking up on me even when we are far away from each other. To **Fredrik Sörén** for being my extra brother and to **Annika Carney** for putting this MD thing in my head.

To **Linda Bonnor** and **Linda Assarsson** for your warm friendship through medical school and thereafter.

To **Alfons**, family and loved ones who did not live to see this day: you are in me.

Populärvetenskaplig sammanfattning

Avhandlingens syfte är att utveckla en metod för datorsimulering av blodflöden som kan förutsäga utkomsten av invasiva ingrepp hos barn med medfödda hjärtfel, och att bedöma hur precisa sådana prediktioner kan vara.

Patientgruppen som studerats är barn med s.k. enkammarhjärtan, där den fungerande kammaren används för att pumpa syresatt blod genom aorta och vidare ut till kroppen. Tillbakaströmmande syrefattigt blod från de stora hålvenerna kopplas på kirurgisk väg förbi hjärtat direkt till lungartärerna som leder till lungorna. Ibland får man göra uppföljande kateterburna eller kirurgiska ingrepp i försök att förbättra blodflödesfördelningen till lungorna. Detta är belastande för det redan sjuka barnet och dess föräldrar, och dessutom resurskrävande. Det skulle därför finnas mycket att vinna om man på förhand kunde räkna ut hur blodflödena blir hos dessa patienter, vilket denna avhandling syftar till.

Fyra arbeten ingår i avhandlingen.

Det första arbetet är en metodstudie som beskriver hur bilder från magnet-resonans (MR) kamera används för att skapa tre-dimensionella modeller för blodflödesberäkning, för barn med enkammarhjärta. Studien innehåller också två patientfall som visar hur metoden kan användas för att förutsäga blodflödet efter ingrepp på de berörda blodkärlen.

Det andra arbetet jämför resultaten från vår metod med en mer avancerad beräkningsmetod, och med resultat från patientspecifika flödesmätningar i MR-kamera. Resultaten visar en betydande tidsbesparing med vår metod jämfört med den avancerade metoden, med beräkningstider som kan minskas från 10-12 timmar till c:a fem minuter utan nämnvärd skillnad i beräkningsresultaten, och med god överensstämmelse med MR-mätningar av blodflöden i patienter.

Det tredje arbetet studerar sambandet mellan andelen blod från levern som når lungorna hos barn med enkammarhjärta, och lungornas egenskaper. Resultaten visar ett tydligt samband mellan fördelningen av leverblodet till lungorna och lungornas resistans och syresättande förmåga. Arbetet innehåller även ett patientfall där prediktiva beräkningar användes för att utforma ingreppet och där utfallet blev som förutsagt.

Det fjärde arbetet studerar metodens prediktiva förmåga för barn som opereras i det sista steget i införandet av cirkulation med enkammarhjärta. Patienterna skannas i MR-kamera dagen före kirurgi, och sedan c:a sex månader efter kirurgi. Resultaten visar god överensstämmelse mellan de prediktiva beräkningarna och mätningarna utförda efter operationen.

Sammanfattningsvis visar avhandlingen att patientspecifika beräkningar kan utföras med god noggrannhet inom en dag från MR-undersökning.

Popular summary in English

The aims of this thesis are to develop a method for computer simulation of blood flow that can predict the outcome of invasive procedures in children with congenital heart disease, and to determine how accurate such predictions are.

The studied group of patients are children with univentricular hearts, where the functional chamber pumps oxygenated blood via the aorta to the rest of the body. The vessels carrying returning deoxygenated blood from the body are surgically connected directly to the pulmonary arteries leading to the lungs, thereby bypassing the heart. Sometimes follow-up invasive procedures are required to improve the blood flow distribution to the lungs. These are hard on the patient and family and are resource intensive. Therefore, there is much to gain if the blood flow to the lungs could be predicted, which indeed is the aim of this thesis.

This thesis is supported by four papers.

The first paper is a method study that describes how images from a magnetic resonance (MR) camera are used to create three-dimensional models for calculations of blood flow. The study also includes two patient cases that show how the method can be used to predict blood flow following invasive changes to the involved blood vessels.

The second paper compares results from our method with a more advanced calculation method, and with patient specific results measured with MR. The results show large time savings with our method compared to the advanced method, with calculation times that could be reduced from 10-12 hours to approximately five minutes with very small differences in the computational results, and with good agreement with MR measurements of blood flow in patients.

The third paper studies the relationship between the amount of blood from the liver that goes to the lungs in children with univentricular hearts, and the function of the lungs. The work also presents a patient case where simulations were used to design an invasive intervention and where the outcome was as predicted.

The fourth paper studies the predictive ability of the method for children operated in the final stage of creating a circulation with a univentricular heart. Patients were scanned in MR on the day before surgery, and approximately six months after. The results show good agreement between the pre-surgical predictions and the results measured in MR after surgery.

In summary, this thesis showed that simulations can predict pulmonary flow in patients with Fontan circulation and that such simulations can be performed within a day of an MRI examination.

1 Introduction

1.1 Overall purpose of this thesis

Congenital heart disease (CHD) is the most common form of birth defect and is the leading cause of mortality in children with congenital malformations. The prevalence of congenital heart defects is reported to be in the range of 8 to 10 per 1000 live births (1–3). While there are countless variants of CHD, modern medicine also provides a wide range of diagnostics and treatment options. In cases where the congenital heart defect is severe, invasive interventions may be required (4,5).

The focus of this thesis is patients with congenital heart malformations resulting in palliation with univentricular heart circulation. To help guide the design of the initial palliation, and when additional invasive interventions are needed to address hemodynamic problems, computational simulations may be helpful in selection and planning of invasive treatment (6–8).

In this context, the overall purpose of this thesis is to help improve the likelihood of successful invasive procedures and reduce the burden of interventions on the patients and on the health care system. The aim is to provide a framework for routine use of predictive computer simulations of pulmonary flow based on data obtained from non-invasive magnetic resonance imaging (MRI).

There are also personal reasons to undertake this work. After fifteen years of international work in the field of mechanical engineering, I attended and graduated from medical school at the Faulty of Medicine, Lund, Sweden. Today, the prospect to combine previous engineering experience with medicine, aimed to help patients with congenital heart disease instils in me a sense of meaning, passion and direction.

1.2 Normal cardiac anatomy and physiology

The human cardiopulmonary system is remarkable in its ability to sustain the needs of the body under near-instantaneous changes in workload as well as in its ability to modify itself in response to longer term changes (9,10).

Contraction of the heart is called systole, and relaxation is called diastole. The normal heart has four chambers: the left atrium (LA), the right atrium (RA), the left

ventricle (LV) and right ventricle (RV) (Figure 1.2.1 A). The right side of the heart provides for the pulmonary circulation in series with the left side of the heart which provides for the systemic circulation. In a healthy adult at rest, the serially connected systemic and pulmonary cardiac output are approximately 5 liters per minute each, which means that the heart as a whole produces 10 liters per minute. Under vigorous exercise, the heart can increase its cardiac output by a factor of five (10).

Deoxygenated blood reaches the heart from the superior vena cava (SVC) and the inferior vena cava (IVC) and enters the RV through the RA and the tricuspid valve. The RV then pumps deoxygenated blood through the pulmonary valve to the lungs (blue path in figure 1.2.1 B). Oxygenated blood returns to the heart from the lungs via the left- and right pulmonary veins to the LA. The LV receives blood from the LA through the mitral valve, and pumps blood across the aortic valve to the body via the aorta (green path in figure 1.2.1 B).

While it was long believed the heart squeezed blood to the body like a clinched fist, the function of the heart is more like a piston. During systole, the atrioventricular (AV) plane between the atria and the ventricles is pulled longitudinally towards the apex, causing systolic ejection of blood from the RV to the main pulmonary artery, and from the LV to the aorta (11). This contraction causes thickening of the ventricular walls, particularly on in the LV, which additionally contributes to the ejected volume. While the heart also has circumferential contraction, longitudinal contraction is the main contributor to stroke volume, producing 80% of the RV stroke volume and 60% of the LV stroke volume, while the total volume of the heart remains relatively constant (12,13).
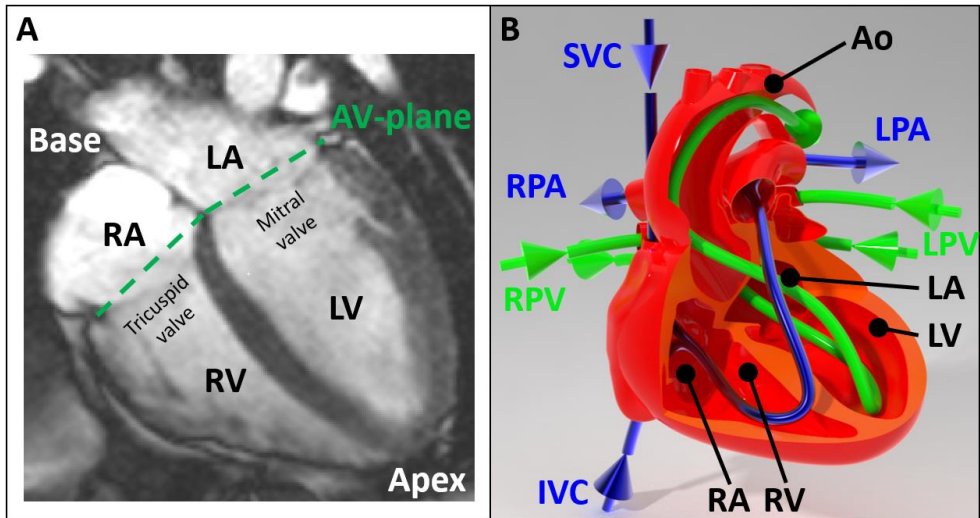
Figure 1.2.1. A normal heart
A: Magnetic resonance imaging four-chamber view of a heart. **B**: Schematic sectioned frontal view of a healthy heart. LV: Left ventricle. RV: Right ventricle. LA: Left atrium. RA: Right atrium. AV-plane: atrioventricular plane. RPA: Right pulmonary artery. LPA: Left pulmonary artery. LPV: Left pulmonary veins. RPV: Right pulmonary veins. IVC: Inferior vena cava. SVC: Superior vena cava. Ao: Aorta. Blue: The path of deoxygenated venous blood from the upper and lower body to the lungs. Green: The path of oxygenated arterial blood from the lungs to the body.

In a healthy heart, filling of the heart occurs to a great extent due to the suction and pressure gradients following relaxation after contraction (14). During systole the AV-valves are closed, and as the AV-plane is pulled toward the apex, blood is sucked into the atria. During diastolic relaxation, blood is sucked into the ventricles as the AV plane springs backward towards the base of the heart. Thus, filling of the atria occurs both during ventricular systole and diastole. Near the end of diastole, the atria contract as well, further pulling the AV plane towards the base. This contributes to the filling of the ventricles, as well as pre-stretching the ventricles to further augment the following ventricular contraction.

Pulmonary resistance is approximately one fifth of systemic resistance (10). Therefore, pulmonary pressure is much lower than in the aorta, and the RV requires less energy to produce the same stroke volume as the LV. In this context we observe that the RV has a much thinner wall than the LV (Figure 1.2.1 A).

The low resistance of the pulmonary vasculature is a prerequisite for passive flow to the lungs, as occurs in the circulation with a univentricular heart, which will be described next.

1.3 Univentricular hearts and the Fontan circulation

Congenital heart defects may occur such that the heart after birth cannot sustain a serial pulmonary and systemic circulation that is conducive to growth and a healthy life. The functional single ventricle provides both pulmonary and systemic circulation in parallel and is volume overloaded (15).

When a biventricular repair aimed to achieve a serial pulmonary and systemic circulation is not possible, implementation of a univentricular heart with a Fontan circulation is a well-established surgical option, named after Dr. Francis Fontan who first demonstrated the principal procedure (16). The aim is to provide the patient with a self-sustained circulation by utilizing the functional ventricle to solely provide for the systemic circulation, with serial pulmonary circulation is provided by passive venous inflow from the caval veins directly to the pulmonary arteries (16,17).

The Fontan circulation is typically introduced in three surgical stages. The first surgery is performed shortly after birth and aims to stabilize the patient while maintaining a mixed venous/arterial circulation with saturation levels conducive to life. The precise procedure depends greatly on the underlying heart defect. In the case of a hypoplastic left heart syndrome (HLHS, Figure 1.3.1 A), a Norwood procedure is performed whereby the right ventricle (RV) pumps to the aorta and unrestricted oxygenated blood flow from the pulmonary veins to the RV is assured with partial resection of the septum between the left and right atrium.

At this stage, the heart has a common ventricle that only pumps to the aorta. Pulmonary circulation is provided via either a Blalock-Taussig (BT) shunt between an aortic branch and a pulmonary artery, or via a Sano-shunt directly from an anterior wall of the ventricle to a pulmonary artery.

The second surgery (often referred to as bidirectional Glenn) is the first step in separating the pulmonary circulation from the systemic circulation and is typically performed 3-6 months after birth. Surgically imposed shunts are taken down and the superior vena cava (SVC) is surgically attached directly to the right pulmonary artery, in what is called a Glenn anastomosis (Figure 1.3.1 B). The pulmonary and systemic circulation are now serial, and the volume loading of the heart is reduced.

The third surgery is typically performed at the age of 18-24 months and aims to also connect the inferior vena cava (IVC) to the pulmonary circulation. The child is then said to have a total cavo-pulmonary connection (TCPC), with the pulmonary circulation completely provided by the passive inflow of all systemic venous blood to the pulmonary arteries. There are variations in the procedure to connect the IVC to the pulmonary arteries. The initial approach by Dr. Fontan (16) utilized the right atrium as a conduit from IVC to the pulmonary arteries. Today, the most common

method is to use an extracardiac GoreTex™ graft as conduit (Figure 1.3.1 B), which has been shown to reduce risk of complications such as arrythmias (18).
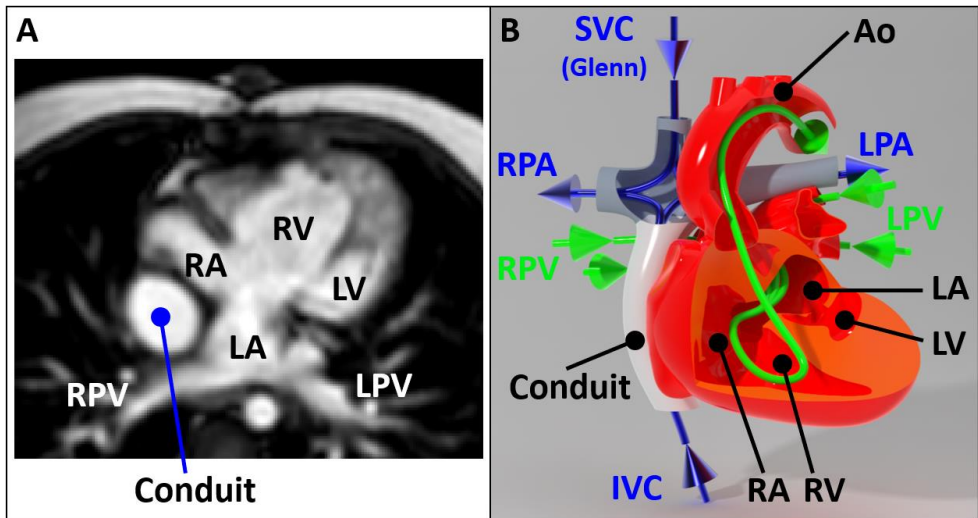
Figure 1.3.1. Univentricular heart with hypoplastic left heart syndrome (HLHS)
A: Magnetic resonance imaging transverse view of a univentricular heart. **B**: Schematic sectioned frontal view of a univentricular heart. LV: Hypoplastic left ventricle. RV: Right ventricle. LA: Left atrium. RA: Right atrium. RPA: Right pulmonary artery. LPA: Left pulmonary artery. LPV: Left pulmonary veins. RPV: Right pulmonary veins. IVC: Inferior vena cava. SVC: Superior vena cava. Ao: Aorta. Blue: deoxygenated venous blood. Green: oxygenated arterial blood.

While many children with univentricular hearts fare well with a transplant free survival after 10 to 20 years in the range of 88-94%, longer 40-year survival has been shown to be around 40% with higher mortality and morbidity seen in patients with right heart morphology (18–22).

There are many known complications due to the heterogenous nature of the original heart defects (23,24). These are often due to altered hemodynamics of the surgically imposed circulation itself, and may result in severe liver fibrosis and cirrhosis, lymphatic congestion, desaturation due to veno-venous collaterals (VVC) or pulmonary arteriovenous malformations (PAVMs) and impaired cardiac output. Complications such as these are often related to elevated central venous pressure and impaired pulmonary hemodynamics. The reduced pulsatility of the venous return has been suggested to adversely affect the vasculature in Fontan patients (25).

The anatomic dimensions and overall design of the Glenn or TCPC anastomosis influence the flow patterns of the blood and therefore the distribution of the pulmonary circulation. It has been shown that unbalanced pulmonary blood flow is associated with worse exercise capacity (26). If a patient develops clinical complications in context of having a narrow pulmonary arteries or related vessel

segments in the Fontan pathway, invasive interventions to dilate narrow sections may be considered (27,28).

Collaterals

Patients with Fontan circulation frequently present with aorto-pulmonary collaterals (APC) that may constitute a significant fraction of the pulmonary perfusion (29–31). APCs often originate from the superior aortic neck vessels such as the subclavian or mammary arteries and diffusely perfuse the pulmonary arterial vasculature. Such collaterals constitute a left to right shunt which increase volume loading on the systemic ventricle (32). While it has been suggested that increased APC flow has no significant effect on the outcome of a Fontan procedure, APC's have been also been associated with longer hospital stay after TCPC surgery as well as poor New York Heart Association functional class (30,33,34). Altogether, the precise significance of APCs and indications for embolization remain of great interest (35–37).

Another form of collaterals are veno-venous collaterals (VVC). VVCs bypass the pulmonary circulation in the Fontan pathway and may thus form a natural fenestration that reduce systemic venous pressure (38).

Hepatic blood

In patients with Fontan circulation, it is widely accepted and observed that a lung that does not receive a certain fraction of the total amount of blood from the liver will develop pulmonary arterial vascular malformations (PAVMs) resulting in intrapulmonary shunting. These shunts bypass the filtering capillary networks of the oxygenating alveoli, causing hypoxia and exercise intolerance (39–44). While the literature mentions that blood from the liver contains "hepatic factors" which are required to maintain pulmonary vascular health, these factors remain unidentified (42,45,46). The literature provides mainly case-related guidance of the relationship between hepatic to pulmonary flow, intrapulmonary shunting and PAVMs (41,47).

1.4 Cardiac Magnetic Resonance Imaging

Magnetic Resonance Imaging (MRI) is a non-invasive, non-ionizing radiological method used to obtain anatomic images, assess cardiac function, measure flow, and obtain quantitative and qualitative tissue characteristics in patients.

While the magnetic field of the MRI scanner is completely harmless to biological tissue, the major safety concern with MRI is presence of magnetic objects in the room which can become dangerous projectiles in the strong magnetic field. Similarly, metal objects inside the body such as pieces of shrapnel or non-MRI

compatible intracerebral clips are additional safety concerns that must be carefully screened for prior to undergoing an MRI examination.

Additionally, the magnetic field can interfere with the function of medical devices such as pacemakers if they are not certified to function in an MRI scanner. Furthermore, the associated radiofrequency (RF) signals can induce heating in pacemaker leads. Some patients may also feel claustrophobic while inside the bore of the scanner.

The magnetic resonance signal

Protons in atomic nuclei are thought of as having a spin-axis with a random orientation relative to a spatial coordinate system. In a strong magnetic field, there is a tendency for the net magnetization of the protons to align with the magnetic field. Furthermore, the net magnetization vector M of the protons will precess with an angular frequency ω around the vector of the external magnetic field B_0 (Figure 1.4.1). The frequency is governed by the strength of the field, according to the Larmor equation,

$$\omega = \gamma \cdot B_0$$

In the Larmor equation, γ is the gyromagnetic ratio, which is specific for the nuclear species. In a typical magnetic field of 1.5 T of an MRI scanner, the net magnetization vector M of protons will precess with a frequency of 64 MHz.

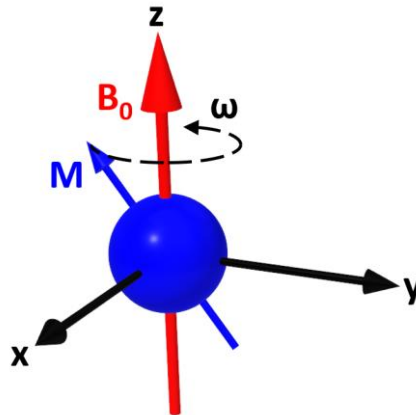**Figure 1.4.1. Spin-axis precession of a proton in a magnetic field**
M: Net magnetization vector. ω: Angular precession frequency. B_0: External magnetic field.

At the iso-centre of the MRI scanner, B_0 is aligned with longitudinal (z) axis of the bore, in which the patient is laying on the scanner bed. The volume of interest in the patient, for example the heart, should ideally be as close to the iso-centre as possible.

Radiofrequency (RF) signals emitted by the MRI scanner at the Larmor frequency will resonate with the protons, causing them to precess in phase around B_0, and the net magnetization vector M will also shift away from B_0 with a flip angle α governed by the energy (time and power) deposited by the RF signal. The magnetization vector M will induce measurable electric signals in receiver coils aligned in the scanner's x-, y- and z-directions. After the RF pulse, the magnetization vector will both de-phase in the x-y-plane and recover alignment with the B_0 direction. The time constant associated with re-alignment along the B_0 direction is called T1, and the time constant associated with de-phasing in the x-y plane is called T2. T1 and T2 are different in different tissues, which allows tissue characterization with the MRI scanner.

Spatial encoding

The MRI scanner has additional, controllable magnetic gradient coils along x-, y- and z-directions of the scanner. If a slight magnetic gradient is applied along the length of the bore (the z-direction), the resonance frequency will be altered depending on the z-location, and therefore an RF pulse in a narrow frequency band can be chosen to select the observed "slice", and the "slice thickness".

Signal encoding in the transverse x-y plane is more complex. In one transverse direction, a magnetic gradient is applied during signal acquisition whereby the received signal magnitude is stronger at frequencies with more protons along the transverse coordinates of the gradient. This is called frequency encoding. Finally, the phase of the RF pulse can be altered along the remaining perpendicular transverse direction. The signal rate of phase change is interpreted as a frequency and is called phase encoding.

At each slice, the collected data is stored in an x-y diagram of "k-space" where the axes are frequencies obtained in the x- and y-direction, and the brightness at each x-y coordinate is the combined magnitude of the signals. An image is created at each slice by graphical superposition of sine signals in the x- and y- direction obtained from reverse Fourier transformation of frequencies and magnitudes in k-space. Low frequencies correspond to large-scale structures, and high frequencies correspond to small, or fine-detailed structures.

The MRI acquisition can be gated by a signal from an electrocardiogram (ECG) to repeatedly aggregate signal from the same phase in the cardiac cycle and obtain images at different time phases over the cardiac cycle. Additionally, MRI acquisition can be gated to occur at a chosen phase of the breathing cycle which can help reduce blurring due to breathing motion.

Measurement of flow

A slice can be selected in a cross-section of interest in a blood vessel. A time-sequenced bipolar gradient of opposing magnitude is given such the magnetization of the first is cancelled by the second. Stationary tissue in the slice will therefore

give no signal. In contrast with stationary tissue, blood entering the slice will aggregate phase as it flows through the slice. The net phase of the signal from within the slice after the bipolar gradient will therefore be proportional to the velocity of the blood. The two-dimensional phase contrast (2D PC) MRI signal is reconstructed as velocity at each pixel in the cross section and integrated across the area of interest, which gives the flow at a given moment in time.

Similarly, four-dimensional phase contrast (4D-PC) MRI signals can be obtained in the x-, y- and z-direction, albeit with lower spatial and temporal resolution to allow data collection within approximately ten minutes (48,49). A three-dimensional velocity vector is obtained at each spatial location and moment in time over a pre-determined volume. 4D-PC MRI thus gives the benefit over 2D-PC MRI that it can be used to retrospectively measure flow at arbitrary locations within the pre-determined volume, even after the patient has left the scanner. In contrast, the locations of 2D-PC MRI measurements must be carefully planned while the patient is in the scanner. Furthermore, 4D-PC MRI can be used to trace the path of virtual particles through blood vessels.

1.5 Patient specific Computational Fluid Dynamics

Broadly speaking, computational fluid dynamics (CFD) is the numerical method by which fluids flow can be computationally evaluated (50). CFD has a vast span of practical applications in different fields of engineering such as turbines, ships, spacecraft, and combustion to name a few. In patient specific simulation related to the hemodynamics of blood flow, the effort typically involves a workflow with a sequence of steps (Figure 1.5.1).

In established CFD methods, the CFD simulation process is often performed using different softwares which require import of data created in the previous step.
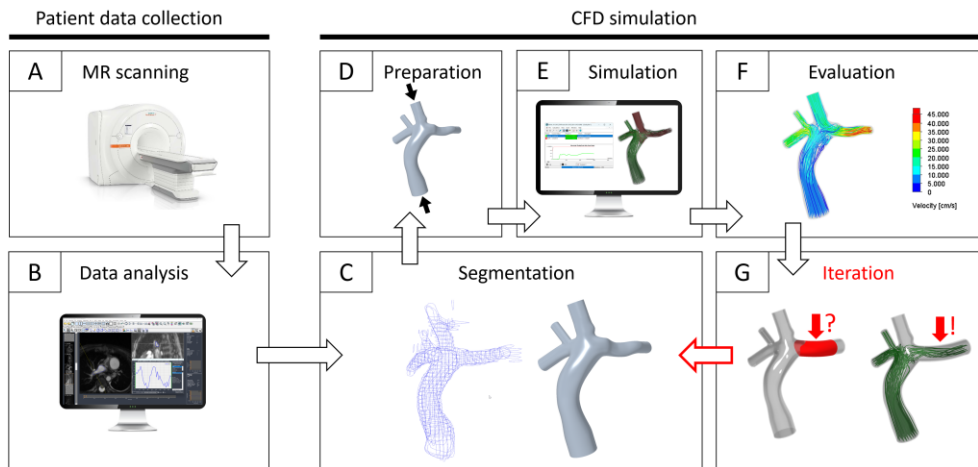
Figure 1.5.1. Steps to create a CFD simulation from MR images
A: MR scanning. **B**: Analysis of MR data. **C**: Segmentation. **D**: Preparation of simulation model. **E**: Performing the simulation. **F**: Evaluation of simulation results. **G**: Modification of model and iteration.

This general workflow for performing a CFD simulation (Figure 1.5.1 C-G) is outlined in more detail as follows.

1.5.1 Segmentation

In the context of CFD simulation, segmentation is the process to create a separate three-dimensional model from information provided by medical imaging, such that this model becomes usable for CFD analysis. Without an adequate geometric model no CFD simulations can be performed. While imaging modalities such as computed tomography (CT) or MRI can obtain patient specific anatomy, three-dimensional ultrasound may also provide detailed local information on for example cardiac valves (51).

Medical imaging data can usually be exported in the Digital Imaging and Communications in Medicine (DICOM) format. The literature mentions several commercial and open-source software packages that can read DICOM data and process it to produce a 3-dimensional model for use in CFD, and for other purposes such as 3D-printing (52,53).

While recent advances in machine learning (ML) have shown promise in automizing the segmentation procedure (54,55), the segmentation process is typically semi-manual or manual.

For semi-manual segmentation, the imaging data is generally required to be isotropic, meaning that the size of each volumetric pixel (voxel) has the same size in the x-, y- and z-direction, and ideally with a resolution of 1 mm or less (53). Once

26

loaded into the segmentation software, areas of interest are separated by thresholding, meaning to select a range of image contrast values that will separate areas of interest from each other, and from areas that should ideally be excluded (Figure 1.5.2 A). Next, manual steps can be performed to isolate objects, remove redundant volumes and smooth surfaces from undesired irregularities (Figure 1.5.2 B, C, D).
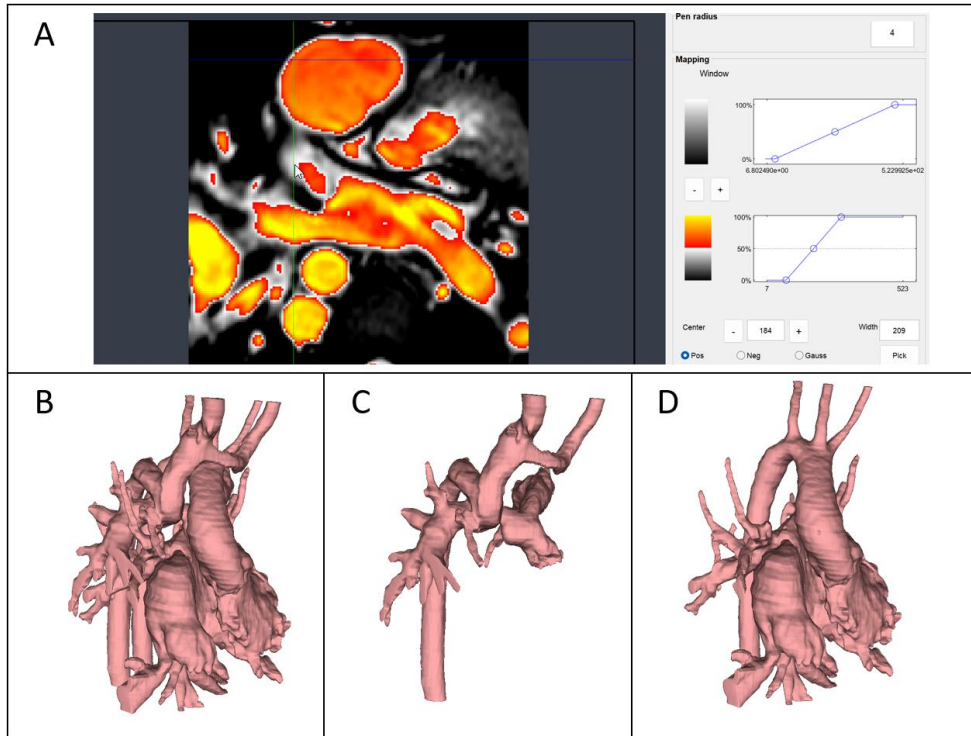
Figure 1.5.2. Segmentation of DICOM data by thresholding
A: Image contrast thresholds are used to separate areas of interest. **B**:Segmentation of pulmonay arteries, heart and aorta in a patient. **C**: Separation of pulmonary arteries. **D**: Separation of heart and aorta. *Screenshots from software Segment 3DPrint, Medviso AB, Lund, Sweden*

While the resulting model in this stage may be adequate for visual purposes or 3D-printing, further use in CFD will require truncating the model at locations corresponding to inlets and outlets. The surface of the final model is represented by a mesh of very small triangular planes, and the surfaces are said to be tessellated.

While some CFD packages can read tessellated files directly, others may require conversion to a smoothed, mathematically defined boundary representation as is used in modern mechanical computer aided design (MCAD) softwares (56–58).

1.5.2   Preparation

Prior to running the simulation, the model is prepared with required CFD-specific information that govern how the model will be solved, given the physiological assumptions of the simulation. In the terminology of computational simulation, this is called pre-processing.

Meshing

The internal volume of the model is spatially discretized into many small volumes called elements; a process commonly referred to as meshing. This process is generally dependent on the type of problem that is to be solved and may require specialized software that is different from the CFD solver software. Local element sizes govern how local changes of flow quantities can be captured during the solution process. Therefore, in areas where the solution is expected to change rapidly over short distances, such as near vessel walls, smaller elements may be required whereas larger elements may provide sufficient accuracy if the local flow is steady at larger scales, for example at the centre of a vessel. High mesh densities will produce more accurate results, at the cost of longer computation times.

Choosing an adequate mesh is therefore a balance between accuracy and solution time. A good modelling practice to find this balance is to perform mesh sensitivity tests. The user runs a model with increasing mesh densities until resulting quantities of interest remain stable within subjectively acceptable limits. If the validation model is principally similar to future models, the user may forego mesh sensitivity tests and apply a previously validated meshing scheme.

In conventional CFD, the elements are aligned with the boundaries of the model, where the solution is known. The discretization of the model with elements is therefore required to conform with geometrical model whose internal volume is of interest in the simulation (50,59).

In contrast, in immersed boundary methods, the elements are not required to conform with the outer boundary. Instead, the solution at the boundaries of the elements is numerically solved such that it counteracts the inner solution of the element, at the boundary of the geometric model. While numerically complex, such approached greatly simplify meshing and may simplify simulated motion of solid structures in the fluid without complex re-meshing algorithms (59,60). The immersed boundary method has previously been used in Fontan CFD simulations (61).

Boundary conditions

A CFD model can only simulate flow in a small fraction of the universe as we know it. The fraction of the universe we choose to simulate is called the simulation domain. While the simulation can calculate values of interest within the simulation domain, such as in a blood vessel in the body of a child, we must provide an

approximation or assumption of what happens at the boundaries of the simulation domain, where the simulation is disconnected from the rest of the world. These are the boundary conditions of the model.

Common boundary conditions in vascular simulation are patient specific, time-averaged, or pulsatile blood flow at the inlets and outlets of the model, often obtained from MRI. Constrained flow at the outlets negates any possibility to analyse changed outlet flows following anatomic interventions on the model.

By instead imposing pressure at the outlets, outlet flow can change at different inlet flow rates and with changed vessel anatomies. Pressure at the outlets can additionally be made dependant of flow rate, flow velocity and net flow volume, representing the resistive, inductive, and capacitive properties of the vasculature distal to the outlets.

Furthermore, the boundary conditions at the outlets and inlets can be connected in a more physiologically complex, closed loop circular system including approximations of the peripheral circulatory system and the function of the heart itself. Such simulations may require a co-simulation, or a separate program or software process representing the peripheral cardiovascular system, running in synchrony with the CFD software, with bi-directional updates between the programs (62,63).

Vessel walls may be approximated as rigid or compliant. Pulsatile pressure may cause compliant vessels to stretch slightly and thereby affect the flow patterns in the vessel lumen. While the effects of such vessel deformation on flow can be analysed numerically and experimentally (64–66), in venous vessels of the Fontan circulation where pressure variability is relatively low, a common approximation is to use rigid vessel walls (61,67,68).

Blood viscosity

Viscosity is the relation between shear stress and shear rate between layers in a fluid volume. Simply put, shear stress (τ) is the traction between two fluid layers, and shear rate is the difference in velocity ($\frac{\partial u}{\partial y}$) between two fluid layers (Figure 1.5.2 A). In blood vessels, velocity transitions from low velocity near the vessel walls to high velocity at the centre of the vessel, and viscosity affects the shape of the flow profile (Figure 1.5.2 B).
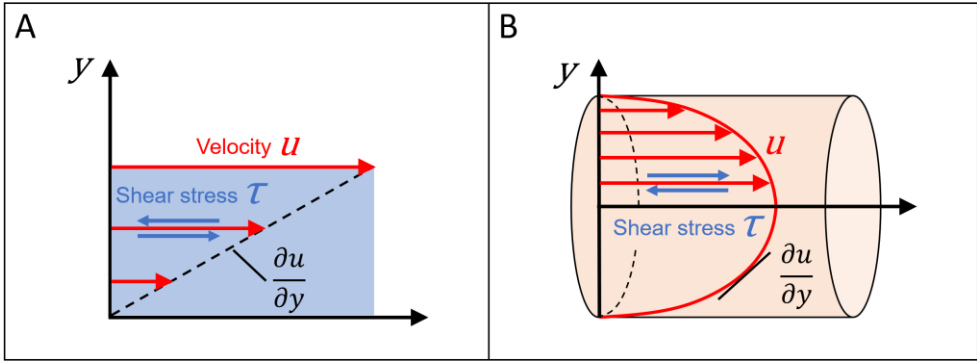
Figure 1.5.2. Shear stress and fluid velocity
A: Over a short distanze (*y*), shear stress (τ) between layers of fluid is proportional to the change of velocity *u* over this distance (∂u/∂y). **B**: In a blood vessel the velocity profile (red) is affected by shear stress between layers of different velocity.

The velocity profile affects the path of blood, and therefore viscosity is of interest in simulations of blood flow in patients with Fontan circulation. In a Newtonian description, viscosity (μ) is approximated as constant according to,

$$\tau = \mu \, \frac{\partial u}{\partial y}$$

Blood is however a bi-phase liquid of cells and plasma, and net viscosity is affected by several parameters such as haematocrit, plasma viscosity and temperature (69). Additionally, interactions between blood cells are different at different shear rates (70). Therefore, blood viscosity may be considered as non-Newtonian fluid where viscosity is not constant. An example of an non-Newtonian fluid approximation is the Carreau model,

$$\eta(\gamma) = \eta_\infty + (\eta_0 - \eta_\infty)[1 + (\gamma\lambda)^2]^{\frac{n-1}{2}}$$

In this formulation, viscosity $\eta(\gamma)$ is dependent on shear rate γ, zero shear viscosity η_0, infinite shear viscosity η_∞, time constant λ and power law index n.

It has indeed been shown that blood exhibits non-Newtonian properties in Fontan patients (71). Both Newtonian and non-Newtonian models have been used in simulations of Fontan blood flow (72–75). A study by Wei *et al.* compared the effect of Newtonian and non-Newtonian blood models on computational hemodynamics in 12 Fontan patients and found only small differences on a population level but large intra-patient differences, as well as computational time savings when using a non-Newtonian model (57).

1.5.3 Simulation

The CFD solution is a numerical and iterative process whereby the governing equations of fluid flow are considered at each fluid element, such that the conservation laws of physics, such as conservation of mass, rate of energy change and rate of change of momentum are preserved locally and globally (50). A central equation within the field of fluid dynamics is the Navier-Stokes equation, which essentially is Newton's second law of motion in context of fluid flow,

$$\rho\left(\frac{\partial \bar{u}}{\partial t} + (\bar{u} \cdot \nabla)\bar{u}\right) = \rho g - \Delta p + \mu \cdot \Delta^2 \bar{u}$$

Here, ρ is density, u is velocity, g is gravity, p is pressure and μ is viscosity. The left side of the equation is mass and acceleration, and the right side is force.

Within each discrete fluid volume, if the sum of quantities which should be preserved are not zero, the remainder is called a residual, which should trend to be lower with each successive iteration if the solution is numerically stable. These residuals are tracked, and the solution is considered converged when residuals are below a subjectively acceptable level. Convergence does however not automatically translate to an accurate solution. An insufficiently discretized model may converge to non-accurate solution. Therefore, a common practice is to test the model at increasing mesh densities until further mesh refinement does not significantly change the solution.

Numerical progression from the current iteration can occur explicitly based only on results from the previous iteration, or implicitly by considering results from both the previous and next iteration. Explicit solutions are generally numerically stable, while they may take longer time since a maximum time-step must be provided. Explicit solutions may be faster at the risk of becoming numerically unstable.

1.5.4 Evaluation

Once the solution is complete, results can be visualized or measured in many various ways. In the terminology of computational simulation, this is called post-processing.

Streamlines show tangential lines of simultaneous velocity vectors in the studied volume at a given moment in time and can be colour coded with any result available at local points within the volume. In the context of hemodynamics, typical measurements used for colour coding are velocity and pressure but there are numerous other parameters that may be visualized.

Pathlines are similar to streamlines in that they show tangential lines of velocity vectors but represent traces of individual particles over the course of time, starting from their release points. As with streamlines, numerous parameters may be visualized. In steady-state simulations, streamlines and pathlines will be identical.

Flow can be measured through user-specified cross-sections of interest.

1.5.5 Iteration

Once results are evaluated and put in context of other clinical information, it may be of interest to change the model and evaluate effects of planned surgical or endovascular interventions aimed at improving patient hemodynamics. As an example, Figure 1.5.1 G shows a hypothetical dilatation of a narrow LPA. Software capable of suitably altering the segmented model is used to modify the anatomy to reflect the planned changes, and the process in steps C – F can be iterated as required to reflect various endovascular or surgical alternatives.

1.6 History and previous research in the field

Studies of simplified models in the form of computational fluid dynamics (CFD) simulations have investigated various placement options of the inferior conduit in relation to the SVC to obtain a reasonable balance between the distribution of blood from the liver to the lungs, and power loss in the anastomosis (73,75,76). Perhaps more importantly, patient-specific computer modelling has proved to be a valuable tool to evaluate various hemodynamic aspects of different anatomical designs at rest and during simulated exercise (8,62,65,67,68,72,77–80).

However, it has been shown that significant resources are required in terms of technical skills, computer power and, not least, calendar lead time to perform such simulations. Trusty *et al.* showed that predictive pre-interventional simulations may require up to a calendar month of lead time, computer simulation time of up to 48 hours, and total work time of 60 hours to simulate just one surgical option at one physiological condition (81).

In this context, research efforts have been directed at finding ways to reduce computational simulation time, with sufficient numerical accuracy and with reasonable physiological approximations, to provide safe and accurate clinical guidance (6,56,57,82–84).

At the time of the writing of this thesis, the total amount of resources required to perform pre-interventional simulations remains a significant hurdle to achieve routine clinical computational support to help guide invasive interventions in children with univentricular hearts (81,85).

2 Aims

The purpose of this thesis was to help improve the likelihood of successful invasive procedures and reduce the burden of interventions on the patients and on the health care system. Therefore, the aim was to provide a framework for fast and routine pre-interventional simulations based on non-invasive MRI in patients with Fontan circulation.

Paper I

The aim was to develop a fundamental method to create CFD simulations from previously acquired non-invasive MRI data, with as little complexity as possible, such that it could be used to predict interventional outcomes. An additional aim was to provide a method to include the effects of aorto-pulmonary collaterals on the distribution of flow to the pulmonary arteries.

Paper II

The aim was to validate results obtained with methods developed in Paper I, with a more advanced and established CFD software, and with flow measurements from MRI. A secondary aim was to determine whether steady-state simulations gave acceptable results compared with simulations performed under pulsatile conditions, and potential time savings thereof.

Paper III

The aim was to establish the relationship between hepatic-to-pulmonary flow and pulmonary vein flow, saturation at rest and simulated pulmonary vascular resistance, such that results of interventional changes on the hepatic-to-pulmonary pathway can be predicted.

Paper IV

The aim was to prospectively determine the predictive capabilities of the previously developed simulation methods by comparing pre-surgical predictions based on MRI on the day before TCPC surgery, with post-surgical MRI measurements obtained approximately six months after surgery.

3 Methods

3.1 Study population

In this thesis, in total 31 patients with univentricular hearts, palliated with either Glenn or TCPC were retrospectively and prospectively included. Some patients were included in more than one study and the overlap is shown in Table 3.1. Patients 12-22 were prospectively included with both Glenn and TCPC palliation, whereas the remainder of the patients were retrospectively included with TCPC palliation. All studies were performed in accordance with approved ethical permissions from the regional ethics review board in Lund, the national ethics review board in Sweden and the principles of the Helsinki declaration.

Paper I

Eleven patients (median age 11 years, age range 3 to 29 years, 3 females) with TCPC palliation who had previously undergone MRI examination were retrospectively included. All patients underwent cardiac catheterization in a dedicated paediatric catheterization laboratory. Six patients had significant aorto-pulmonary collaterals (APC), defined as pulmonary vein flow that exceeded pulmonary artery flow. This was supported by findings from catheterization, with visible collaterals and saturation step-up in the distal pulmonary arteries (86).

Patient 4 underwent a subsequent stent dilatation of LPA, and patient 3 underwent a surgical implantation of a Y-graft intended to evenly distribute blood from the liver to LPA and RPA. Both patients underwent post-interventional MRI.

Paper II

Nine of the eleven patients from Paper I were included (median age 11 years, age range 3 to 17 years, 2 females). One of the patients from Paper I was excluded due to a severely dilated atrium used as conduit from VCI to RPA, which made tracking of hepatic blood from VCI to the pulmonary arteries unfeasible. Another patient from Paper I was excluded due to reversed flow in LPA due to APC inflow. This pre-determined that all hepatic blood from IVC flowed to RPA and was therefore not a meaningful result for the study, which aimed to simulate the distribution of hepatic blood. Additionally, 6 patients (median age 2.5 years, age range 2.3 to 3.1 years, 3 females) with Glenn palliation were prospectively included.

Paper III

Eighteen patients with TCPC palliation (median age 7 years, age range 3 to 14 years, 8 females) were included, whereof nine were prospectively included. An experienced reader in paediatric radiology, blinded from the simulation results, examined MRI, CT, and catheterization images for presence of veno-venous collaterals (VVCs) and pulmonary arteriovenous malformations (PAVMs). Two patients were found to have VVCs draining to the pulmonary veins, and two other patients were previously diagnosed with PAVMs. Patient 31 underwent a staged, minimally invasive endovascular intervention aimed at redirecting some of the blood from the liver veins towards the left lung.

Paper IV

Eleven patients (median age 2.5 years, age range 1.8 to 8.3 years, six females) with Glenn palliation were prospectively included to a pre-surgical MRI scan prior to TCPC surgery, and a follow-up MRI scan planned to occur six months after surgery. Due to the Covid19 pandemic, median follow-up time was 9 months, range 1 to 18 months. Patient 18 was re-admitted for MRI after one month due to low arterial saturation and was successfully treated with a stent dilatation of LPA and administration of sildenafil due to high net pulmonary resistance in the left lung. Patient 21 was readmitted after one month due to pulmonary effusions and was successfully treated with invasive drainage.

Table 3.1. Patient inclusion in the studies

TCPC: Total cavo-pulmonary connection. (*) Dextrocardia, left isomerism, bilateral Glenn/Kawashima, azygos continuation of VCI, liver veins to LPA. DILV: Double inlet left ventricle. ccTGA: congenitally corrected transposition of the great arteries. PS: pulmonary stenosis. DORV: Double outlet right ventricle. VSD: ventricle septum defect. HLHS: hypoplastil left heart syndrome. PA/IVS: pulmonary atresia, intact ventricular septum. HRHS: hypoplastic right heart syndrome. MS: mitral stenosis. AVSD: atrio ventricular septum defect. (**) HLHS, left isomerism, bilateral Glenn/Kawashima, azygos continuation of VCI, main pulmonary artery towards LPA. (***) HLHS, left isomerism, bilateral Glenn/Kawashima, azygos continuation of VCI, liver veins to RPA.. VCI: vena cava inferior. LPA: left pulmonary artery. RPA: right pulmonary artery.

Patient	Paper I	Paper II	Paper III	Paper IV	Diagnosis	Sex	Age at MRI
1	TCPC	TCPC			DILV, TGA, PS	M	3
2	TCPC	TCPC			DORV, VSD, PS	M	16
3	TCPC	TCPC			(*)	F	11
4	TCPC	TCPC			DORV, VSD	M	3
5	TCPC	TCPC			DORV, TGA	M	17
6	TCPC	TCPC			HLHS	M	4
7	TCPC	TCPC			TGA, VSD	F	13
8	TCPC	TCPC			HLHS	M	11
9	TCPC				PA/IVS, HRHS	M	10
10	TCPC	TCPC			AVSD, TGA, PA	M	3
11	TCPC				TA	M	29
12		Glenn	TCPC	Glenn, TCPC	DILV, PA, VSD	M	2.5, 3
13		Glenn	TCPC	Glenn, TCPC	PA/IVS	F	3.1, 3.5
14		Glenn	TCPC	Glenn, TCPC	HLHS	M	1.8, 3.2
15		Glenn	TCPC	Glenn, TCPC	HLHS	F	2.8, 3.5
16		Glenn	TCPC	Glenn, TCPC	PA/IVS	F	2.3, 4.5
17		Glenn	TCPC	Glenn, TCPC	HLHS	F	2.1, 2.9
18			TCPC	Glenn, TCPC	(**)	M	8.3, 8.4
19			TCPC	Glenn, TCPC	DORV, AVSD	F	2.5, 3.5
20			TCPC	Glenn, TCPC	HLHS	M	2.3, 3
21				Glenn, TCPC	ccTGA, VSD, PA	M	2.6, 2.8
22				Glenn, TCPC	DORV, ccTGA, VSD	F	3.5, 4.4
23			TCPC		HLHS	F	7
24			TCPC		TA, HRHS	M	12
25			TCPC		HLHS	M	13
26			TCPC		HLHS	M	12
27			TCPC		HLHS	M	15
28			TCPC		PA, VSD, HRHS	M	12
29			TCPC		PA, TGA	F	14
30			TCPC		MS, VSD	M	8
31			TCPC		(***)	F	14

3.2 Magnetic resonance imaging

Magnetic resonance imaging (MRI) was used to obtain anatomic images, cine images and flow measurements under free breathing in all patients.

Patients 1-11 (Table 3.1) were scanned in a 1.5 T Philips Achieva (Philips Healthcare, Best, The Netherlands). Patients 12-31 (Table 3.1) were scanned in a 1.5 T Siemens Aera (Siemens Healthineers, Erlangen, Germany). Patient 3 underwent pre-interventional MRI in the Philips Achieva and, following surgical implantation of a Y-graft (Figure 4.1 C-D), post-interventional MRI in the Siemens Aera. Some, but not all patients underwent four-dimensional phase contrast (4D PC) MRI, validated in vivo, in vitro, and in large and small vessels (48,87–89). Typical MRI sequence parameters are shown in Table 3.2.

For the purposes of clinical method development, additional sequences were performed when there was opportunity to do so, such as a T2-weighted sequence for visualization of lymphatic pathways, which provided data that was not explicitly used in this thesis.

Patients need to lie still in the scanner for the duration of the examination, which may take up to an hour. Therefore, the young prospectively included patients (patients 12-22, Table 3.1) were sedated with intranasal administration of dexmedetomidine. The first dose of dexmedetomidine (100 µg/ml), 2-3 µg/kg, was given approximately 40 minutes prior to start of examination. A second dose of 1 µg/kg was given at the start of the examination. A paediatric cardiologist was on call during all examinations where dexmedetomidine was administered. There were no complications related to sedation or the MRI examinations.

Table 3.2. Magnetic resonance imaging parameters
bSSSP: balanced steady state free precession. TR: recovery time. TE: echo time. VENC: velocity encoding. 2D-PC: two-dimensional phase contrast. 4D-PC: four-dimensional phase contrast

Scanner	Philips Achieva	Siemens Aera
bSSFP cine		
TR / TE/ Flip angle	2.9 ms / 1.5 ms / 60˚	40 ms / 1.4 ms / 51˚
Slice thickness	5 mm	4-5 mm
In-plane resolution	1.2 x 1.2 mm	1 x 1 mm
2D-PC flow measurement		
TR / TE/ Flip angle	10 ms / 6.5 ms / 15 ˚	40 ms / 2.6 ms / 20 ˚
In-plane resolution	1.2 x 1.2 mm	2 x 2 mm
VENC	Aorta: 200 cm / s Other vessels: 80 cm /s	Aorta: 200 cm / s Other vessels: 80 cm /s
4D-PC flow measurement		
TR / TE/ Flip angle	6.2 ms / 3.6 ms / 8˚	46 ms / 3.5 ms / 8˚
Spatial resolution	3 x 3 x 3 mm	3 x 3 x 3 mm
VENC	100 cm / s	50-100 cm / s

3.3 Computational fluid dynamics

A method was developed using commercial software, aiming to provide a workflow for safe, predictive pre-interventional CFD simulations with minimum complexity and minimum required lead time.

In Paper II, this process was titled "lean" in the sense of its aim to minimize wasteful steps and embrace continuous improvement. Results of this process were compared with results from a more established method which may be considered more accurate, or at least more widely adopted by expert CFD users. The steps to perform these processes follow the steps in Figure 1.5.1 and are outlined as follows.

3.3.1 The "Lean" CFD method

Many patients in this thesis were retrospectively included and scanned according to routine clinical MRI protocols, with anatomical sequences of 1 x 1 x 5 mm resolution in three projections. This resolution is not sufficient for semi-manual segmentation (Figure 1.5.2).

Thus, a process was developed for manual segmentation based on vessel contours. Manually drawn endocardial contours is the clinical standard to obtain cardiac volumes and function and has been used to obtain accurate volumes of other organs such as kidneys and even foetuses (12,13,55,90–92).

The software Segment (Medviso AB, Lund, Sweden) (92) was used to draw contours of blood vessels from multiple projections. The contours were imported to Creo Parametric (PTC, Boston, MA, USA) and used as reference to fit a three-dimensional model (Figure 3.3.1.1) (58).
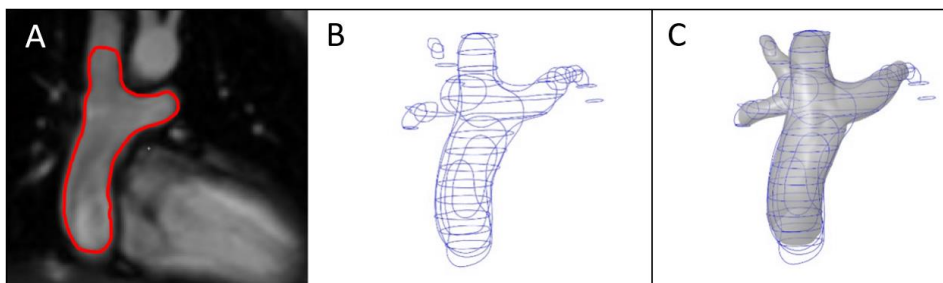

Figure 3.3.1.1. 3D segmentation from vessel contours
A: Delineation of vessel contours in a coronal projection **B**: Vessel contours in multiple sections and projections. **C**: Reconstruction of the vessel by placing surfaces at the contours using mechanical computer aided design software. *Image adapted from Frieberg et al.* (58)*, John Wiley & Sons, through a CC BY 4.0 license (https://creativecommons.org/licenses/by/4.0/).*

MRI artifacts from stents can negate any possibility of contour-based segmentation in the affected areas. In these cases, images obtained from fluoroscopic angiography during stent or device implantation were used to reveal vessel boundaries as shown in Figure 3.3.1.2 (58).
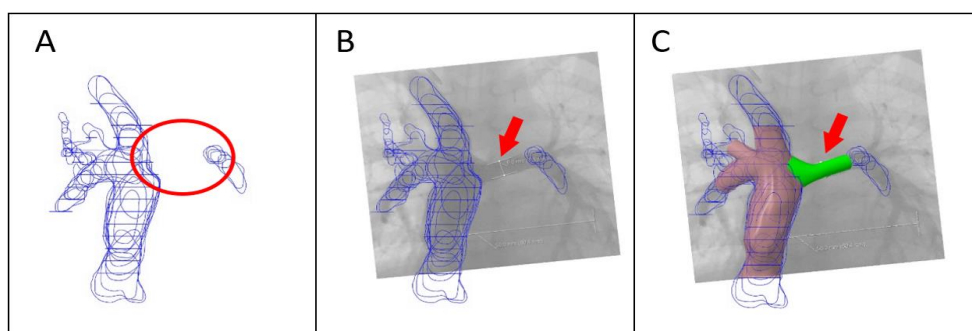
Figure 3.3.1.2. 3D segmentation in areas with stent-induced signal loss
A: MRI signal loss due to a stent partially prevented segmentation (red circle). **B**: A superimposed fluoroscopic angiogram shows the contours of the stented vessel (red arrow). **C**: Reconstruction of the stented area (red arrow). *Image adapted from Frieberg et al.* (58)*, John Wiley & Sons, through a CC BY 4.0 license (https://creativecommons.org/licenses/by/4.0/).*

In patient 18, input from an isotropic white-blood sequence was used to semi-manually segment the vessels and was used as reference to fit a three-dimensional model in Creo Parametric (Figure 3.3.1.3).
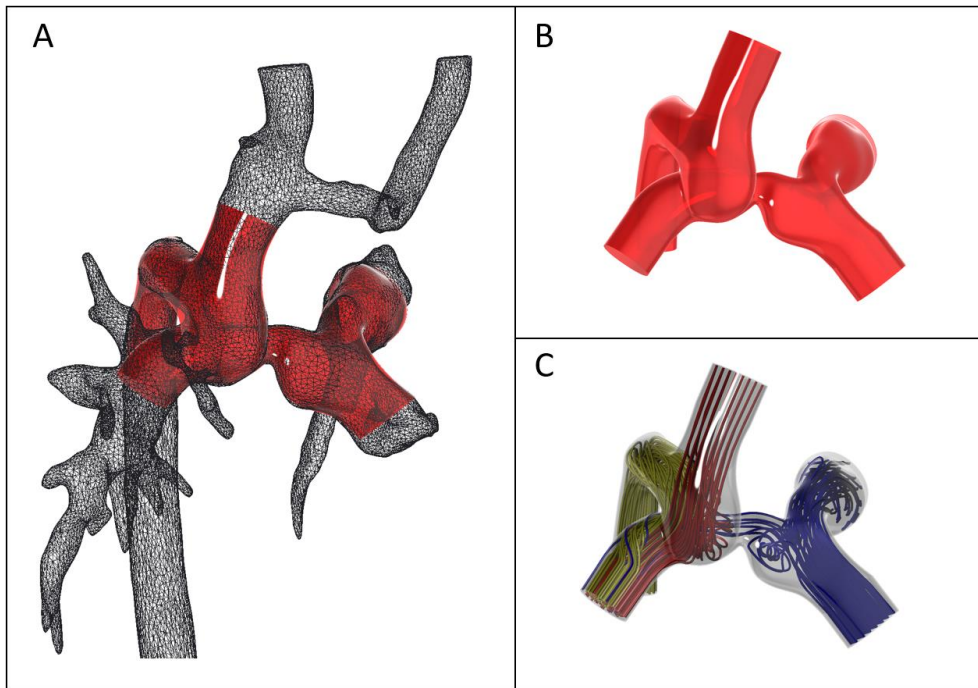

Figure 3.3.1.3. Conversion of a tesselated surface model to a smooth boundary representation
A: Tesselated model of pulmonary arteries in a patient (black) and mechanical computer aided design (MCAD) model (red). **B**: MCAD model of proximal pulmonary arteries. **C**: Flow simulation created from MCAD model.

Preparation, simulation and evaluation (Figure 1.5.1 D-F) of the CFD model was performed in Simcenter FloEFD for Creo (Siemens EDA, Wilsonville, OR, USA), which is embedded in the Creo Parametric user interface. FloEFD has a unit-management system which allows medical units of flow (l/min), volume (ml), pressure (mmHg) and velocity (cm/s) etc, when data is entered to the software.

Patient-specific flows obtained from MRI were placed at the inlets of the model, typically at the superior vena cava (SVC) and inferior vena cava (IVC). Pulmonary vascular resistance was simulated with thin, porous baffles (93) placed proximally to the extended pulmonary artery outlets. These porosities satisfy the fundamental linear resistive equation $\Delta p = R \cdot F$, where Δp is the transpulmonary gradient, R is pulmonary vascular resistance and F is pulmonary flow.

Meshing was performed in FloEFD. Mesh sensitivity studies performed in Paper II showed that mesh-independent results were obtained with approximately 150000 elements for TCPC patients and 140000 elements for Glenn patients. In Paper I, automatic mesh refinement during the ongoing simulation was explored but was found to provide little effect on results over a sufficiently dense mesh to begin with.

Simulation was performed with the immersed boundary solver of FloEFD, with the assumption of rigid walls with no-slip boundary conditions. The default internal convergence algorithms were used for both steady-state and pulsatile simulations. Additionally, all user-defined measurements, such as outlet flows, percentage of total- and hepatic flow to LPA and power loss were tracked for convergence. All simulations were performed with non-Newtonian viscosity.

When the solution was complete, all FloEFD results were visualized within the Creo user interface. We titled the method "lean" since it seemed resource sparse.

Iteration

Paper I, III and IV included patient cases where anatomies were modified to represent invasive interventions. In the integration between Creo Parametric and FloEFD, all settings and boundary conditions, including the geometric references they are attached to, were maintained following modifications to the geometry.

3.3.2 The "Established" reference CFD method

In Paper II, the results from the previously described Lean method were compared with those obtained from Star CCM+ (Siemens PLM Software, Plano, TX, US), which was considered an established CFD method for hemodynamic calculations (84,94–97).

Previously reconstructed models were exported from Creo Parametric to the neutral geometric IGES file format and imported to ICEM CFD (Ansys Inc, Canonsburg, PA, USA) for meshing. The mesh was scaled to SI-units and imported to Star CCM+. Following a systematic mesh convergence study, mesh-independent results were found with approximately 1.6 million elements in TCPC patients, and with 1.1 million elements in Glenn patients, with previously described meshing procedures (98,99). Great care was taken was taken to correctly translate patient-specific boundary conditions to SI-units.

Convergence was considered achieved when residuals were below 10^{-5}. In pulsatile simulations, 4000 time steps per cardiac cycle were used. Six cardiac cycles were performed in both softwares, such that flow from IVC via the conduit to LPA reached a cyclic steady state in the last cardiac cycle, from which results were obtained.

Results were visualized in the Star CCM+ user interface.

3.4 Hemodynamic measurements

In this thesis, several hemodynamic measurements obtained from MRI and CFD were used. Most of these were used in Paper II to compare numerical results produced by FloEFD and Star CCM+. A brief overview of these measurements and how they were obtained are presented as follows.

Pulmonary flow distribution to the left pulmonary artery (%LPA)

$$\%LPA = \frac{Q_{LPA}}{Q_{LPA} + Q_{RPA}} \cdot 100\%$$

Q_{LPA} and Q_{RPA} are the left and right pulmonary artery flow, respectively, as measured in MRI or CFD.

Hepatic Flow Distribution to the left pulmonary artery (%HFD)

$$\%HFD = \frac{Q_{IVC\ to\ LPA}}{Q_{IVC}} \cdot 100\%$$

Q_{IVC} is the IVC flow. $Q_{IVC\ to\ LPA}$ is the flow from IVC directed to LPA, as measured in CFD (Figure 3.4).
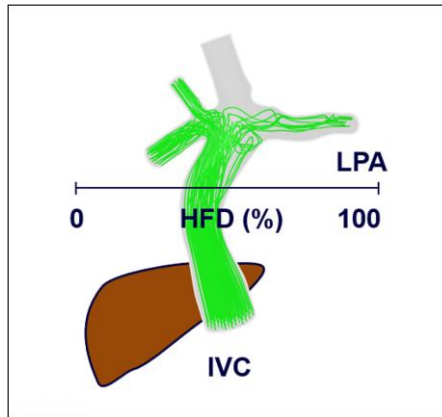

Figure 3.4. Definition of the hepatic to left pulmonary artery percentage (HFD)
100% HFD means that all of the blood from the inferior vena cava (IVC) goes to the left pulmonary artery (LPA). 0% HFD means that all IVC blood goes to the opposite side.

Power Loss ($\dot{E}_{loss}$)

$$\dot{E}_{loss} = \sum_{inlets\ A} \int (p + \frac{1}{2}\rho v^2)v \cdot dA - \sum_{outlets\ A} \int (p + \frac{1}{2}\rho v^2)v \cdot dA$$

Power loss is the difference between power entering at the inlets and exiting at the outlets of the studied volume (78). In short, power is calculated as flow multiplied by the sum of static and dynamic pressure. p is the static pressure, ρ is the blood density, v is the velocity and A is the cross-section area of the respective inlets and outlets.

Wall Shear Stress, WSS (τ_w):

$$\tau_w = \mu \frac{\partial u}{\partial y}$$

WSS can be visualized on the vessel walls of the CFD model. μ is the dynamic viscosity and $\partial u / \partial y$ is the rate of shear.

Time Average Wall Shear Stress (TAWSS)

$$TAWSS = \frac{1}{T} \int_0^T |\tau_w|\, dt$$

TAWSS is the average wall shear stress over one heartbeat and can be visualized on the vessel walls of the CFD model. T is the physical time of one heartbeat and τ_w is the local wall shear stress.

Pulsatile Index (PI)

$$PI = \frac{Q_{max} - Q_{min}}{2 \times Q_{avg}} \times 100\%$$

Q_{max}, Q_{min} and Q_{avg} are the maximum, minimum and average flow rates at a vessel cross-section, as measured in MRI (100).

Weighted Pulsatile Index (wPI)

$$wPI = \sum_{i=1\ldots n} PI_i \times C_i$$

WPI represents the overall pulsatility of the Fontan connection (100). C_i is the relative flow split of vessel i and is calculated as $C_i = Q_i/Q_{mean}$, where Q_i is the flow in vessel i, and Q_{mean} is the average flow in all vessels.

Normalized Wall Shear Stress Area

This was calculated using CFD as the ratio of the area with WSS or TAWSS < 0.4 Pa, compared to the total vessel wall area. This measure has been suggested to be associated with increased risk of atherosclerosis and thrombosis (101,102), and has been previously reported in Fontan patients (56).

3.5 Simulation of resistance and collaterals

Paper I and II

In paper I and II, the presence of aortopulmonary collaterals (APC) were dichotomized as either being present or not. APC flow was quantified as the difference between pulmonary vein flow and pulmonary artery flow, as measured in MRI (31,103). Moreover, a previous paper which studied the same eleven patients additionally used findings from cardiac catheterization such as visually enlarged aortopulmonary collaterals and saturation step-up in the distal pulmonary arteries (86).

APCs enter the pulmonary artery circulation through many, and often diffuse pathways. While it was briefly explored, it was found impractical to include physical inlets of APC flow to the pulmonary arteries of the simulation models. As a proxy for the presence of APCs, a method was instead devised to increase simulated pulmonary vascular resistance with a factor corresponding to the increase of total pulmonary flow due to inflow of APCs. With the example of flows in the left pulmonary artery (LPA) and the left pulmonary vein (LPV), the net resistance as used the in simulations (R') was scaled based on pulmonary flows and "intrinsic" pulmonary resistance R (Figure 3.5.1).

According to Figure 3.5.1 the trans-pulmonary gradient p_1 - p_0 can be written in two ways,

$$p_1 - p_0 = (Q_{LPA} + Q_{APC})\,R$$

…and…

$$p_1 - p_0 = Q_{LPA}\, R'$$

These formulations were combined to obtain a simulated net resistance R' which was used as a proxy for the inclusion of collaterals distal to the outlets of the simulation model:

$$R' = R\, \frac{Q_{LPA} + Q_{APC}}{Q_{LPA}}$$

Assuming no veno-venous collateral contributions to pulmonary vein flow, Q_{LPA} + Q_{APC} is pulmonary vein flow (Q_{LPV}). Thus, simulated net resistance as used in the simulations (R') becomes R' = R · (Q_{LPV}/Q_{RPA}). Q_{LPV} and Q_{LPA} were obtained from MRI. What remained was to choose R.

While catheterized pressures and resistance can be calculated from catheterization, we aimed to provide a simulation framework for distribution of pulmonary flow based on non-invasive measurements of anatomy and flow obtained from MRI.

The literature reports total PVR in 4-year-old patients with univentricular hearts to be in the range of 0.9 – 5.3 Wood Units, (WU, mmHg·l^{-1}·min) (104,105). In this Paper I and II, we uniformly chose an intrinsic R of 1.5 WU for each lung, which is in the low range of physiological PVR.
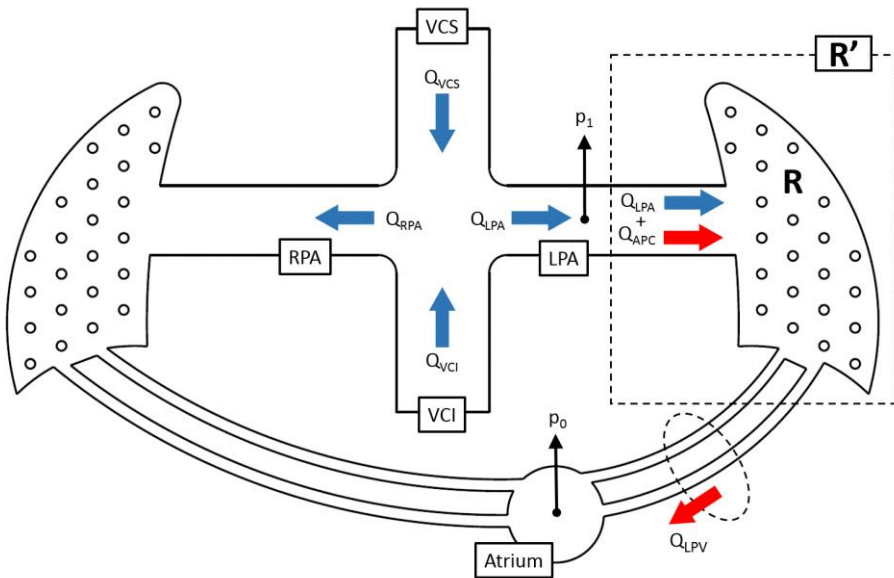
Figure 3.5.1.Schematic overview of a total cavo-pulmonary connection (TCPC)
Schematic overview of a total cavo-pulmonary connection (TCPC), including the vena cava superior (VCS), the vena cava inferior (VCI), the right pulmonary artery (RPA) and the left pulmonary artery (LPA). The figure shows the MRI flow measurements used to account for and simulate the effects of aorto-pulmonary collaterals on the TCPC flow distribution. Q denotes flow, R resistance and R´net resistance.

Paper III

In paper III, the method for including aortopulmonary collaterals was extended to include parameterization of simulated pulmonary vascular resistance (PVR) in each lung, respectively. This way, the simulations were used to change simulated PVR in each lung such that there was a perfect match between pulmonary artery flow measured in CFD simulations and MRI.

The ratio of left to right simulated PVR in each lung was parameterized such that total intrinsic PVR of both lungs was 1.5 Wood Units (WU). Total intrinsic PVR (PVR_{tot}) was calculated from simulated left- and right PVR ($PVR_{left,sim}$ and $PVR_{right,sim}$) according to:

$$\frac{1}{PVR_{tot}} = \frac{1}{1.5} = \frac{1}{PVR_{left,sim}} + \frac{1}{PVR_{right,sim}}$$

The ratio of left:right simulated PVR was then iterated in CFD in the patient-specific CFD models until pulmonary artery flow in CFD agreed with patient-specific MRI measurements of pulmonary artery flow.
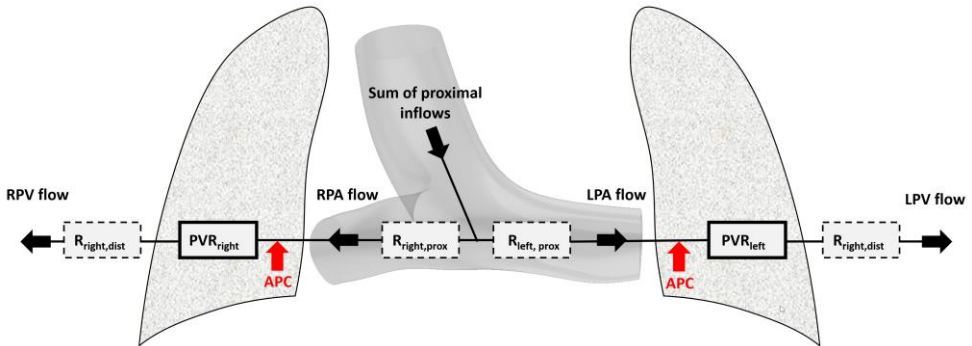
Figure 3.5.2.Schematic overview of resistances in the pulmonary pathway
Thick boxes show the inner resistance of the lungs. Dashed boxes show proximal and distal resistances. PVR: Pulmonary vascular resistance. RPA: Right pulmonary artery. RPV: Right pulmonary vein. LPA: Left pulmnary artery. LPV: Left pulmonary vein.

With this information, we hypothesized that if the simulated flow distribution was identical to corresponding measurements in MRI, the relation between simulated left and right PVR may be a proxy for the corresponding ratio of in-vivo PVR.

With the definitions from Figure 3.5.2, given the simplified assumption that:

$$PVR_{right} \gg R_{right,prox} + R_{right,dist}$$

and…

$$PVR_{left} \gg R_{left,prox} + R_{left,dist}$$

…then Ohms law provides a relationship between PVR and pulmonary vein flow as follows:

$$\frac{PVR_{left}}{PVR_{right}} = \frac{RPV\ flow}{LPV\ flow}$$

Thus, we hypothesized that the relation between pulmonary vein flows as measured in MRI is another proxy for the corresponding ratio of in-vivo PVR. Here, an obvious confounder is distal contribution to pulmonary vein flow, such as from veno-venous collaterals (VVCs). An experienced paediatric radiologist blinded from MRI and CFD measurements reviewed available radiologic data to find visual evidence of such contributions.

Paper IV

Pre-interventional MRI was planned on the day before planned TCPC surgery. Glenn anatomies were simulated in CFD and the ratio of left:right simulated PVR was iterated as previously described such that pulmonary artery flow in the simulations matched the observed pulmonary artery flow in MRI.

Based on information from the performing surgeon, a hypothetical conduit was inserted into the models between the insertion of the inferior vena cava (IVC) and the right atrium, and the planned anastomosis on the pulmonary arteries. Predictive simulations were performed with inflows from the pre-interventional MRI, and with unchanged resistances from the pre-interventional simulation.

After the follow-up MRI, new patient specific CFD models were created from scratch and the simulated left- and right pulmonary resistances were tuned as previously described such that simulated pulmonary artery flow matched the observed pulmonary artery flow in MRI.

4 Results and comments

4.1 Paper I

In the complete group of eleven patients, the percentage of pulmonary flow to the left pulmonary artery (LPA%) as measured in CFD, agreed with the corresponding measurement in MRI with a correlation coefficient r = 0.79 (p=0.004). Bias was 2.9 ± 5.3% (Figure 4.1.1).
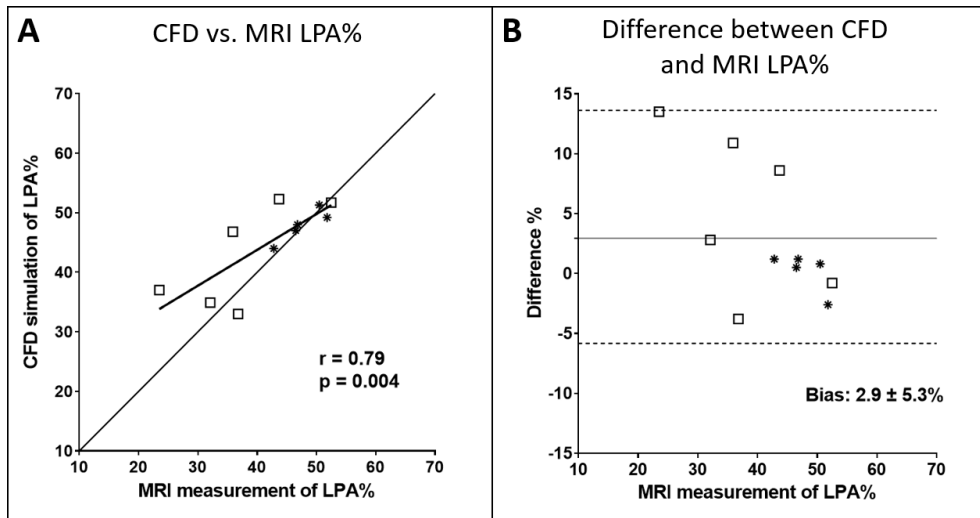
Figure 4.1.1. Regression of MRI measurements and computational fluid dynamics (CFD) simulations
A: Regression showing MRI and CFD measurements of left pulmonary artery flow percentage (LPA%) for the 11 patients. **B**: Modified Bland Altman plot with the difference between MRI and CFD on the vertical axis. Open square data points represent patients with APC. *Figure adapted from Frieberg et al.* (58)*, John Wiley & Sons, through a CC BY 4.0 license (https://creativecommons.org/licenses/by/4.0/).*

Additionally, among the six patients with identified aorto-pulmonary collateral (APC) flow, bias was 5.2 ± 6.3% when the simulated pulmonary vascular resistances were adjusted for APC flow, and 9.8 ± 7.0% with no adjustments for APC flow. This suggested that effects from competitive inflow due to APC in the distal pulmonary vasculature can be compensated for in simulations, by adjustment

of the simulated pulmonary vascular resistance based on flows non-invasively obtained from MRI.

Results from the two patients who had undergone invasive interventions were as follows.

One patient underwent a stent dilatation of LPA from six to eight millimetres. In CFD, pre-interventional inflows and boundary conditions were maintained, and the only change was the dilatation of LPA. The pre-interventional flow to LPA was 32.6% in CFD, and 30.2% in MRI. Post-interventional flow was 34.9% in CFD and 32.1% in MRI. Thus, CFD predicted a 2% increase of flow to LPA, which was also observed in MRI (Figure 4.1.2 A-B).

We found good visual agreement between the segmented model created from MRI contours, and fluoroscopic angiograms obtained during stent insertion and dilatation (Figure 3.3.1.2). While this was not a complete validation of the segmentation method, at least these results suggested that the 3D-models were reasonably correct. Also, with vessel contours from angiograms superimposed on the 3D model, the complete model could be constructed in areas with MRI artefacts due to the metallic stents.

The second patient underwent an open surgery implantation of a Y-graft (18 + 9 + 9 mm) intended to improve flow from the liver to the right lung. The Y-graft was applied to the pre-surgical anatomy, with maintained pre-surgical inflows from MRI. This simulation was performed after surgery, a few days before the patient underwent post-interventional MRI.

CFD results showed that there was no flow in the right limb of the Y-graft (Figure 4.1.2 C). The CFD findings agreed with the post-surgical MRI, which showed that there was no flow in the right limb of the Y-graft (Figure 4.1.2 D).

These results suggested that simulations based mainly on pre-interventional, non-invasive MRI could predict post-interventional outcomes.
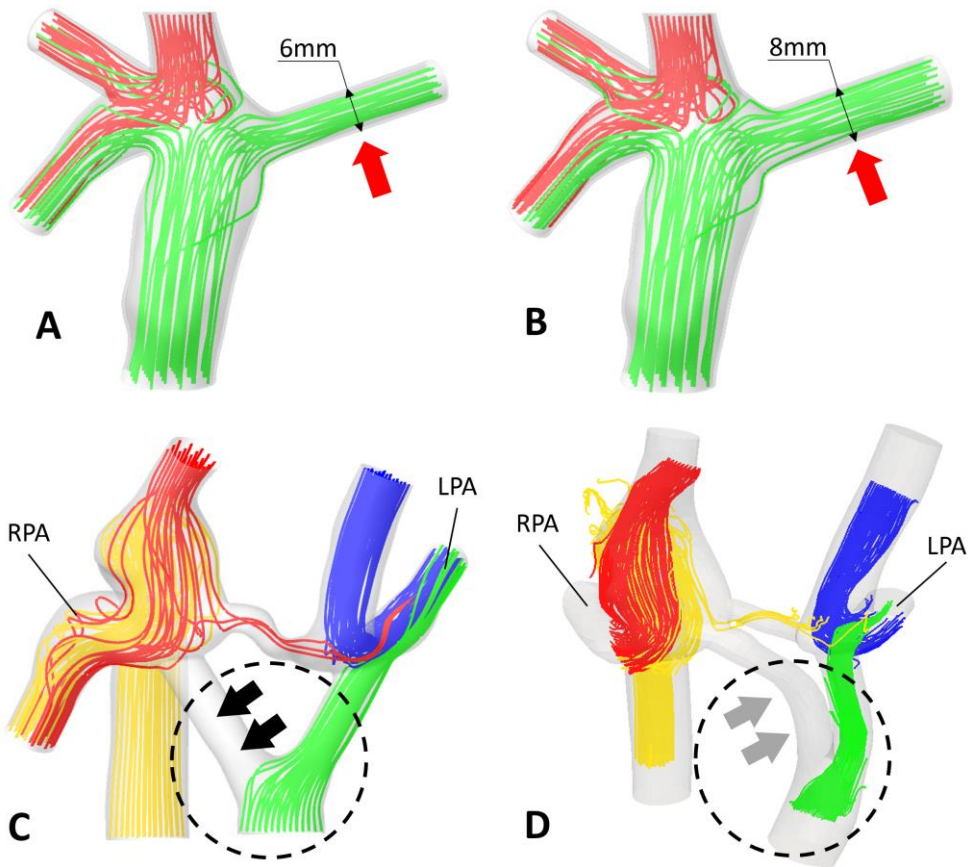
Figure 4.1.2. Computational fluid dynamics (CFD) simulation of interventions
CFD simulation of a stent dilatation from 6mm (**A**) to 8mm (**B**) predicted a 2.3%-unit increase of LPA flow and the MRI showed a 1.9%-unit increase of LPA flow after intervention. In another patient, a y-shaped graft (**C** and **D**, dashed circles) was surgically implanted to divide the flow from the liver to both lungs. The CFD model (**C**) predicted that flow to the right lung in the inserted y-graft would be near zero (C, black arrows). 4D-flow from the post-operative MRI (**D**, grey arrows) confirmed the CFD modeling results. *Figure adapted from Frieberg et al.* (58)*, John Wiley & Sons, through a CC BY 4.0 license (https://creativecommons.org/licenses/by/4.0/).*

4.2 Paper II

While we previously found good agreement in our simulations with flow observed in MRI, and between CFD predictions of post-interventional flow and post-interventional flow observed in MRI (58), the use of our software had not been previously reported in Fontan simulations. Moreover, we noted that our computer for CFD simulation was relatively less powerful than computers used in other studies (58,106,107).

Thus, a validation of the subjectively "lean" software with an "established" CFD software was undertaken. We aimed to reveal differences in user work times, simulation times and results with both softwares, under steady state and pulsatile flow conditions, using identical anatomies, boundary conditions and rheology.

The lean software was Simcenter FloEFD for Creo (Siemens EDA, Wilsonville, OR, USA). The established software was Star CCM+ (Siemens PLM Software, Plano, TX, US). The process to create and perform the simulations in both softwares was optimized to minimize user work time and simulation time, while not compromising solution accuracy.

Results showed very similar visual flow patterns in the lean software and the established software (Figure 4.2.1). Visual agreement was also found in results of wall shear stress (WSS), both under steady state, and pulsatile conditions between both softwares (Figure 4.2.2).

Regression of all quantified results from the hypothesised least accurate solutions (steady state lean simulations) with the hypothesized most accurate solutions (pulsatile established simulations), as well as Bland-Altman analyses all showed high correlation and low bias (Figure 4.2.3).

Figure 4.2.1. Velocity-coded streamlines
Patients with TCPC (Above) and Glenn (Below). Results are shown from the lean CFD with steady-state flow, established CFD with steady-state flow, and established CFD with pulsatile flow. *Image adapted from Frieberg et al. (108), Springer, through a CC BY 4.0 license (https://creativecommons.org/licenses/by/4.0/).*

As seen in Figure 4.2.2 all simulations showed similar distributions of wall shear stress (WSS). In this work, a WSS of 0.4 Pa was used as reference. In simulations of WSS in patients with Y-grafts (similar to patient 3, Figure 4.1.2 C-D), thrombosis was reported in a Y-graft limb when WSS was approximately 0.5 Pa (68).
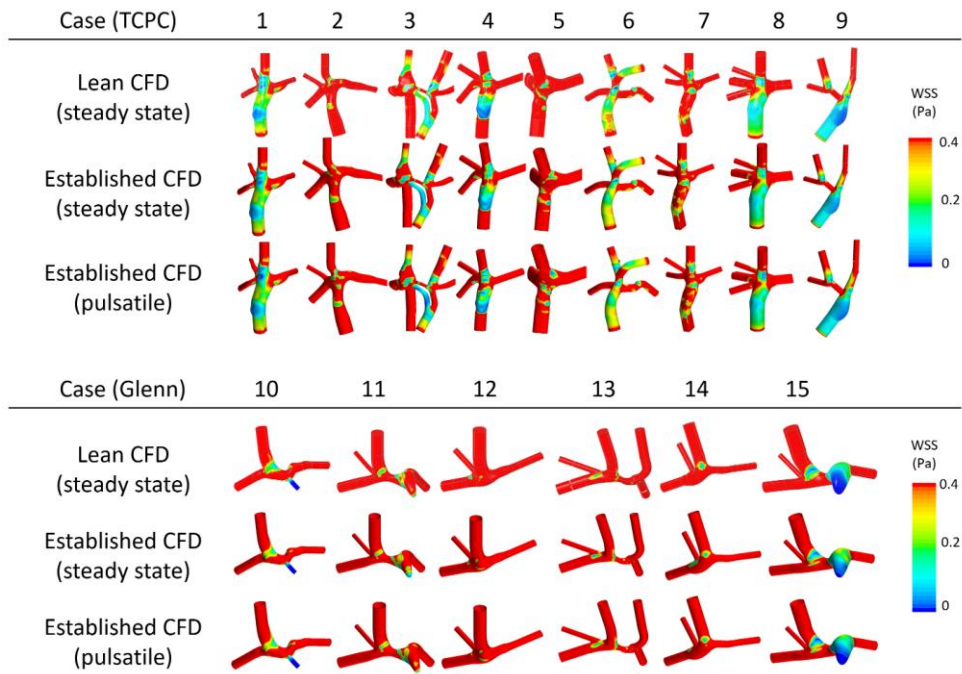
Figure 4.2.2. Contour plots of the wall shear stress (WSS) and time averaged WSS
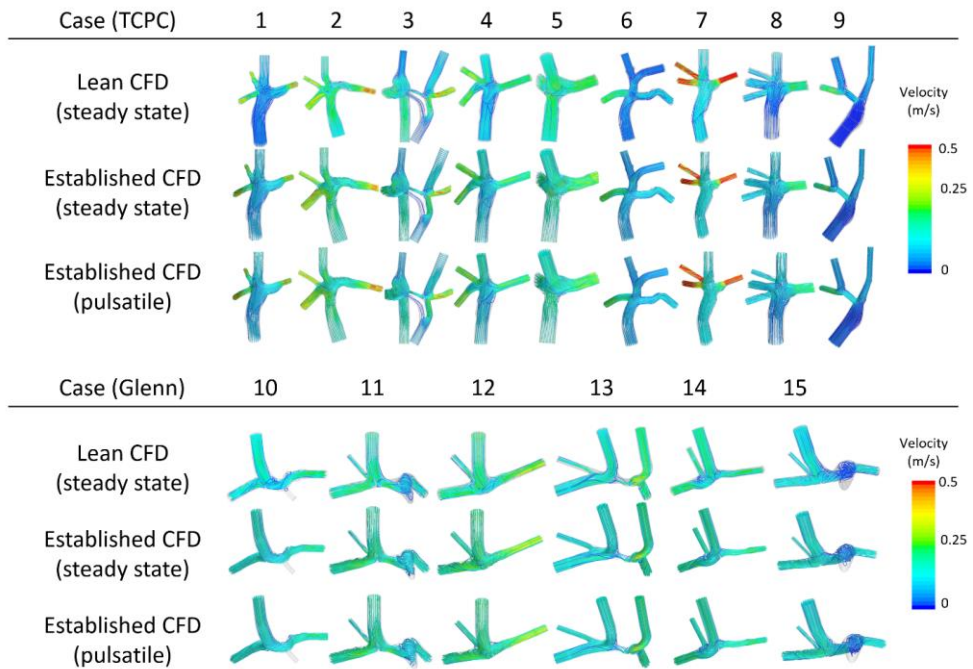Patients with TCPC (Above) and Glenn (Below). Results are shown from the lean CFD with steady-state flow, established CFD with steady-state flow, and established CFD with pulsatile flow, showing time-averaged wall shear stress. Red areas show wall shear stress >0.4 Pa. *Image adapted from Frieberg et al. (108), Springer, through a CC BY 4.0 license (https://creativecommons.org/licenses/by/4.0/).*

Table 4.2. User work time and computer solver time in minutes, mean±SD

Patient group	User work time in minutes, mean±SD (seconds in parenthesis)				Computer solver time in minutes, mean±SD (hours in parenthesis)			
	Lean CFD		Established CFD		Lean CFD		Established CFD	
	Meshing	CFD settings	Meshing	CFD settings	Steady	Pulsatile	Steady	Pulsatile
TCPC	<1	15±3	23±4.3	34±3.4	3.7±2.3	75±29 (1.3±0.5h)	34±12	570±115 (9.5±1.9h)
Glenn	<1	15±3	19±3.3	31±7.7	2.0±0.6	17±3.3	11±4.2	203±65 (3.4±1.1h)
All	(10±2.8 s)	15±3	21±4.1	33±5.6	3.0±2.0	52±36	25±15	421±203 (7.0±3.4h)
					Workstation 8 cores		Server 32 cores	
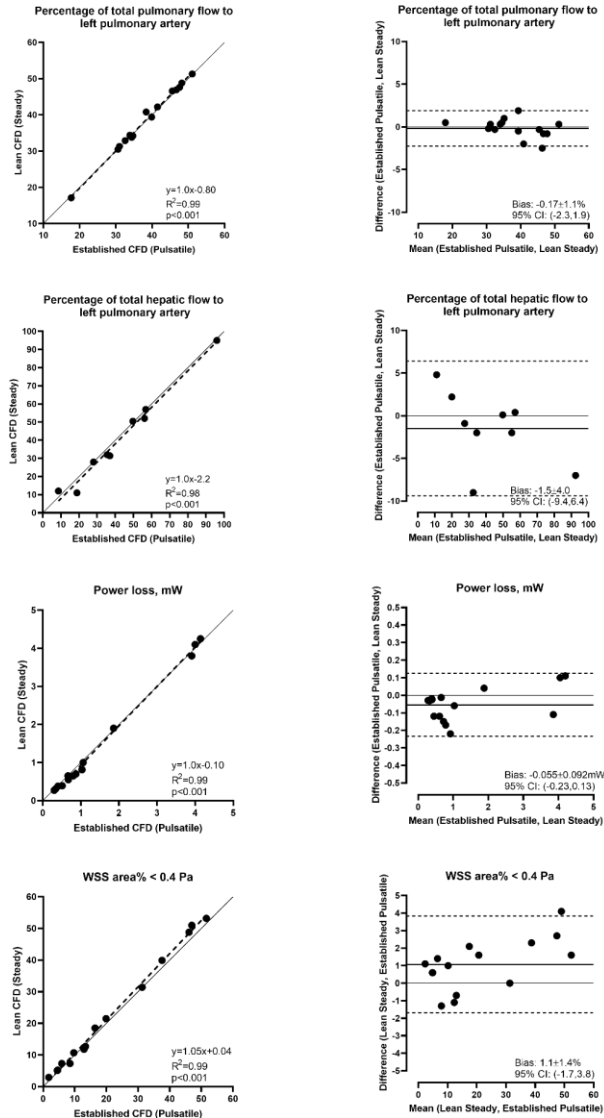
Figure 4.2.3. Regression of results obtained from the Lean and the Established simulation tools
First row: Linear regression (Left) and Bland-Altman analysis (Right) of total flow distribution to left pulmonary artery, comparing steady state lean CFD with pulsatile established CFD. **Second row**: Linear regression (Left) and Bland-Altman analysis (Right) of hepatic flow distribution to left pulmonary artery, comparing steady state lean CFD with pulsatile established CFD. **Third row**: Linear regression (Left) and Bland-Altman analysis (Right) of power loss, comparing steady state lean CFD with pulsatile established CFD. **Fourth row**: Linear regression (Left) and Bland-Altman analysis (Right) of normalized WSS area, comparing lean steady state results with established pulsatile CFD results. *Image from Frieberg et al.* (108)*, Springer Nature, through a CC BY 4.0 license (https://creativecommons.org/licenses/by/4.0/).*

The major differences in results from the lean and established software were found in computer solver times and the user work times (Table 4.2).

The computer solver time was much shorter with the lean method, with steady-state computation times of 3 minutes and pulsatile simulation times of 52 minutes. In contrast, the established method required 25 minutes for steady-state computations and seven to ten hours for pulsatile simulations. Provided with identical geometries to begin with, we found the user work time to prepare a CFD model was 15 minutes with the lean approach, and 35 minutes with the established approach.

4.3 Paper III

Papers I and II (58,108) used assumptions of bilaterally constant pulmonary vascular resistance. This was a clear simplification, and it is known that many factors may affect pulmonary vascular resistance (PVR) in each lung.

One such factor is the distribution of hepatic blood from the liver (HFD) via the inferior vena cava (IVC) and the total cavo-pulmonary connection (TCPC) conduit to the lungs. Maldistribution of such blood which contains yet unidentified "hepatic factors" is known to cause pulmonary arteriovenous malformations (PAVMs) (42–44) and intrapulmonary shunting in the lung that receives too little of these substances. Indeed, among the studied patients, two patients were diagnosed with PAVMs, as indicated by the blue arrows in Figure 4.3.1.

Regressions of simulated IVC flow to the left pulmonary artery (HFD) with the simulated ratio of left:right PVR and the in-vivo measurements of right:left pulmonary vein flow as proxies for the ratio of left:right in-vivo PVR suggest that HFD explains 47-50% of PVR (Figure 4.3.1 A-B).

While clearly influenced by values at the extreme ends, quadratic regression of simulated IVC flow to left pulmonary artery (HFD) with saturation at rest (SpO_2) suggested that HFD explains 56% of SpO_2 (Figure 4.3.1 C). Exclusion of the extreme values resulted in a coefficient of determination $R^2 = 0.15$.

Two patients were previously diagnosed with PAVMs (Figure 4.3.1, blue arrows). One of these patients underwent a staged, minimally invasive intervention aimed to increase the amount of hepatic blood to the left lung (Figure 4.3.2). Numerous invasive alternatives were explored using CFD prior to selection of the planned intervention. With the proposed intervention, simulations predicted an increase of HFD from 7% to 20%. Notably, one CFD simulation was performed during the on-going final intervention.

Post-interventional MRI confirmed that HFD increased to 20%, as predicted by CFD. Furthermore, post-interventional changes in simulated PVR, pulmonary vein

flow and SpO2 remained within the confidence intervals of the cohort (Figure 4.3.1, red arrows), and at follow-up MRIs (Figure 4.3.2). This suggests predictive capabilities of the findings from the cohort.
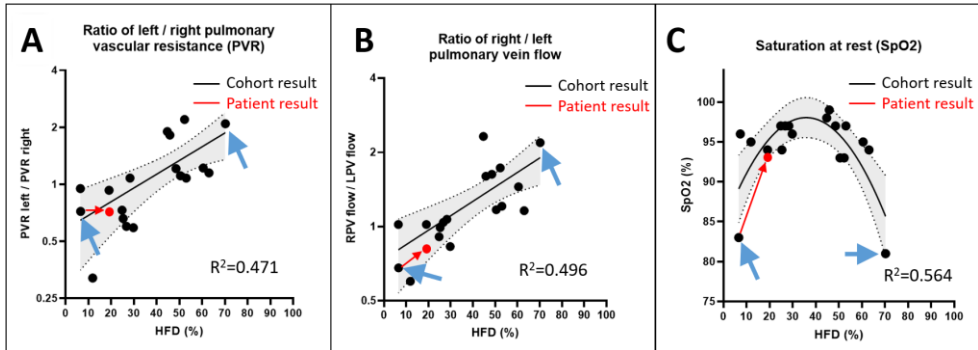

Figure 4.3.1. Regressions
A: Regression of the fraction of hepatic flow to the left pulmonary artery (HFD) with the left/right ratio of pulmonary vascular resistance (PVR). **B**: Regression of the fraction of hepatic flow to the left pulmonary artery (HFD) with the ratio of right/left pulmonary vein flow. **C**: Regression of the fraction of hepatic flow to the left pulmonary artery (HFD) with saturation at rest (SpO2). These Regressions may potentially be used to predict outcome in these parameters following interventions that change the hepatic flow distribution. Grey area: 95% confidence interval. Red arrows indicate post-interventional change in one patient. Blue arrows indicate patients diagnosed with pulmonary arteriovenous malformations (PAVMs).
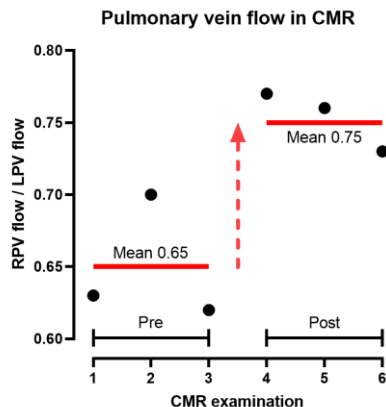
Figure 4.3.2. Pre- and post-interventional pulmonary vein flow.
The graph shows how the right / left pulmonary vein flow ratio changed in the interventional patient from a mean of 0.65 during three pre-interventional CMR examinations, to a mean of 0.75 during over the course of three post-interventional CMR examinations. *CMR*: cardiovascular magnetic imaging. *RPV*: Right pulmonary vein. *LPV*: Left pulmonary vein. Dashed arrow: time of final intervention.
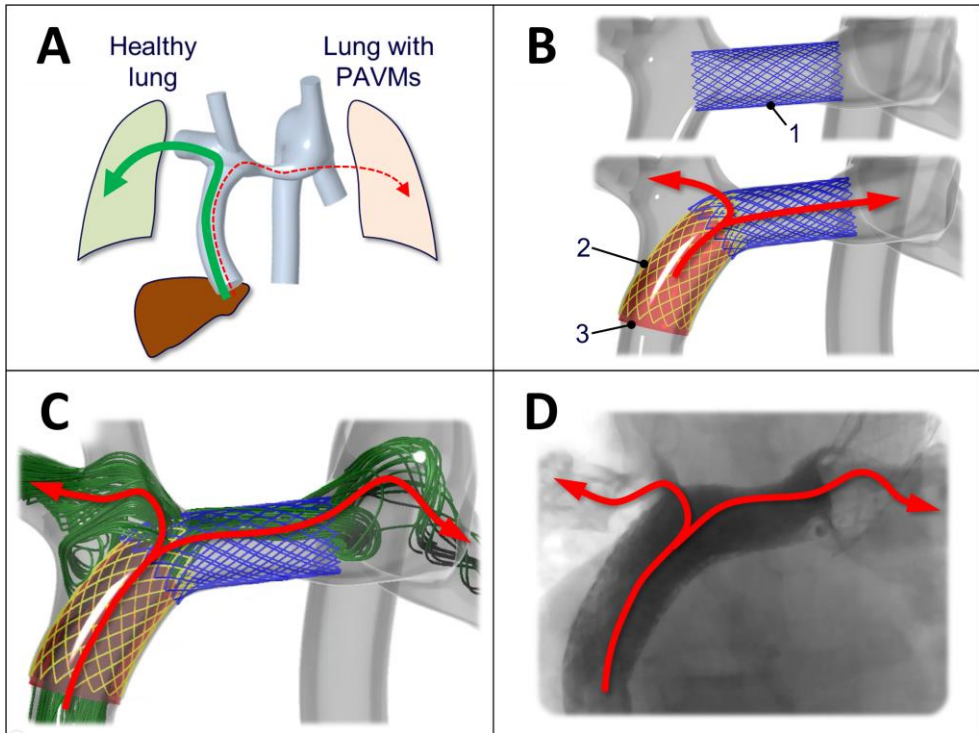
Figure 4.3.2. Patient with intervention
A: Patient with hepatic blood flowing mainly to the left right lung and pulmonary arterio-venous malformations (PAVMs) in the left lung. **B:** Proposed staged endovascular intervention to improve hepatic flow to the left lung. 1: open cell stent in central pulmonary artery. 2-3: open cell stent into conduit with internal covered stent, leaving a fenestration for hepatic blood to flow to the right lung. **C:** Pre-interventional simulation of proposed stenting. **D:** Post-interventional fluoroscopic angiogram which showed good agreement between contrast flow and the pre-interventional simulation.

Of note, the median ratio of right to left pulmonary vein flow in the patients was 1.11, compared with approximately 1.07 as reported in healthy adults (109).

4.4 Paper IV

In this study, 11 patients were prospectively included to a pre-surgical MRI on the day before planned TCPC surgery, and a post-surgical MRI approximately six months after surgery.

Based on data from the pre-interventional MRI, CFD simulations of both the pre-surgical Glenn and predictive simulations including the planned placement of the conduit were performed in a timeframe such that the operating surgeon could be

informed prior to start of surgery on the day after MRI. All predictive simulations were performed with maintained pre-interventional boundary conditions from MRI, and pre-interventional simulated pulmonary vascular resistances (PVR).

Due in part to the Covid pandemic, some patients had later follow-up MRI than planned. In two patients, MRI was performed earlier than in the protocol because of clinical indications for MRI. In total, the range of follow-up MRI was 1-18 months.

As seen in Figure 4.4.1, with one notable exception, the predicted conduit placements compared reasonably well with the actual placement of the conduits, as segmented from the post-interventional MRI.

Regression of the predicted and actual inferior vena cava to left pulmonary artery flow fraction (HFD) showed a correlation r = 0.73 (p = 0.01). Bias according to Bland-Altman analysis was 8.2 ± 17% (Figure 4.4.2 A-B). A post-hoc adjustment of the location of the conduit in the patient indicated by the black arrow in Figure 4.4.1 and 4.4.2 changed the correlation of IVC flow to LPA to r = 0.92 (p < 0.001), and bias to 2.8 ± 8.3 %.

Regression of the predicted and actual total pulmonary flow fraction to the left pulmonary artery showed a low correlation of r = 0.13 (p = 0.71). The low bias of -4.3 ± 11% suggested that the total pulmonary artery distribution did not change much post-operatively (Figure 4.4.2 A-B).

Our study presented the opportunity to study post-surgical changes in pulmonary and systemic hemodynamics as measured in MRI. We found a lower aorto-pulmonary collateral (APC) flow post-surgically, as measured by the difference between pulmonary artery and pulmonary vein flow. Pre-surgical APC flow decreased from 0.6 (0.4 – 1.4) to 0.5 (0.2 – 0.9) $l \cdot min^{-1} \cdot m^{-2}$ (p = 0.02), similar to the findings of Latus *et al.* who in 51 follow-up MRIs found a decrease from 0.52 (0 - 2.8) to 0.37 (0 - 2.9) $l \cdot min^{-1} \cdot m^{-2}$ (median and range) (37).

Additionally, cardiac index decreased from 3.4 ± 0.39 to 2.9 ± 0.31 $l \cdot min^{-1} \cdot m^{-2}$ compared to pre-interventional measurements (p = 0.032).
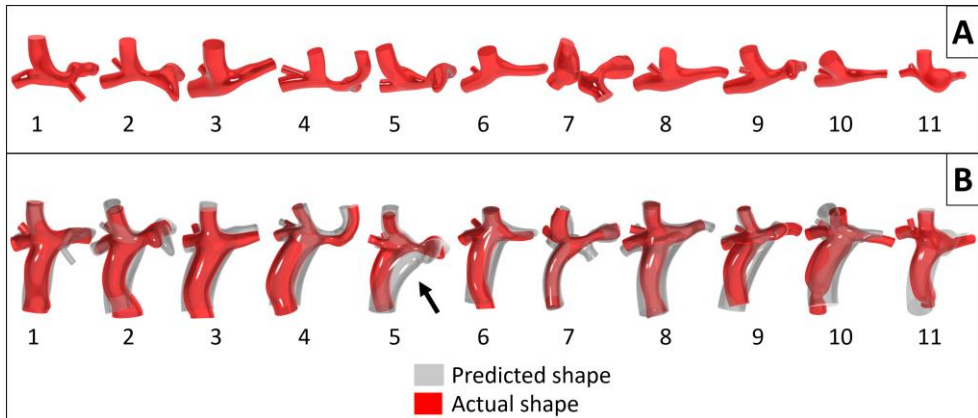
Figure 4.4.1. Pre- and post-interventional anatomies

A: Models of the pre-interventional (Glenn) pulmonary artery anatomies. **B**: The predicted post-interventional (TCPC) pulmonary artery anatomies are shown in gray and the actual post-interventional anatomies are shown in red. The arrow shows the patient with the greatest visual difference between predicted and actual conduit anatomy. TCPC: total cavo-pulmonary connection.
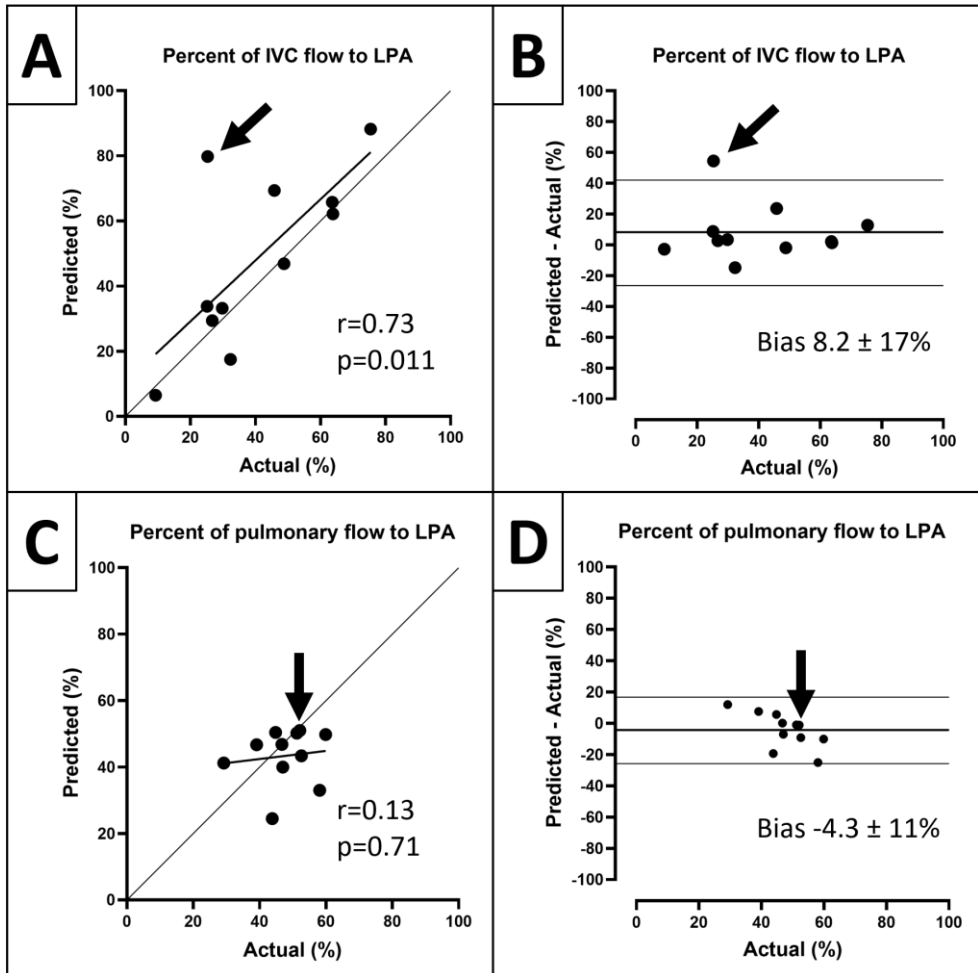
Figure 4.4.2. Regressions and bias of predicted versus actual pulmonary flow
A: Regression of the predicted versus actual percentage of inferior vena cava (IVC) flow to the left pulmonary artery (LPA). **B**: Bland Altman plot of the predicted versus actual percentage of IVC flow to LPA. **C**: Regression of the predicted versus actual total pulmonary flow to LPA. **D**: Bland Altman plot of the predicted versus actual total pulmonary flow to LPA. The arrows indicate patient 5 who had the greatest visual difference between predicted and actual conduit anatomy.

5 Discussion

One major finding of this thesis is that pre-interventional simulations can be routinely performed with vastly shorter lead times than has been previously reported.

Indeed, we have showed that both an MRI scan and patient-specific simulations can be routinely performed on the day before planned surgery, in contrast with up to a month of lead time with simulation time of up to 48 hours (81). Our findings showed that accurate simulation results using time-averaged flow can be obtained with solution times in the scale of 3-10 minutes on a standard computer, compared with up to 10 hours using six cycles of pulsatile flow with a more established CFD method running on a much faster computer (108).

These results should be placed in context of recent publications which explored various CFD solver techniques aimed to reduce computation times (82–84). While the used computer hardware or user work times were not disclosed, Liu *et al.* showed CFD simulation times as low as 9.4 minutes with steady-state boundary conditions, and with good agreement between CFD results and in-vitro experiments (83).

An important aspect to save time that has not previously been considered is the required effort to modify a patient-specific model such that it represents a proposed invasive intervention. In the "lean" method, the software that can modify the geometry and perform the simulation are integrated in the same user interface. While the initial segmentation and preparation takes approximately 1-2 hours, we found that simple geometric changes followed by re-simulation can both be performed in the time scale of minutes. This means that the "lean" method may be suitable to perform complementary simulations to address questions raised during on-going invasive interventions.

Additionally, we prospectively studied the predictive capabilities of proposed methods, which showed that pre-interventional predictions performed on the day before TCPC surgery can predict the total- and hepatic-to-pulmonary flow distribution, as measured by MRI and CFD between 1 and 18 months after surgery.

Our finding of predictive versus actual HFD bias of $8.2 \pm 17\%$ was very similar to the recently reported bias of 17 ± 13 % by Trusty *et al.* (110). While that study did not report used hardware or computation times, pulsatile flows were used with 20

cardiac cycles. We speculate that the lead time and computation time were in the range of those previously reported, namely approximately one calendar month and 48 hours, respectively (81). In contrast, in our study MRI and predictive simulations were both performed in less than a day, with computation times of approximately ten minutes.

Another recent publication by Wei *et al.* (85) conclude that "the clinical usage of Fontan simulation is hindered by the low computational efficiency of current methods", and that "efforts to reduce simulation uncertainties and enhance computational efficiency could significantly promote the routine application of these simulations". We believe this thesis addresses these obstacles.

Furthermore, we have for the first time demonstrated the relationship between hepatic-to-pulmonary flow, pulmonary vein flow and oxygen saturation at rest. This suggests that in many cases, surgeons and interventionists can effectively choose which pulmonary flow distribution they would like to achieve, given the simulated optimal placement of the inferior conduit to the pulmonary arteries.

Altogether, the findings of this thesis should be seen in context of the centralization of highly specialized tertiary referral centres where invasive interventions in children with congenital heart disease are performed. With availability of MRI in combination with routine and rapid predictive simulations, there may be time to evaluate many invasive options after the patient has arrived for elective invasive procedures. While potentially improving patient care, this may also save cost of care for the facility as well as time and cost of travel for the family.

5.1 Limitations

In Paper I and II, fixed values of pulmonary vascular resistance (PVR) were chosen, whereas we know for a fact that PVR is not constant and is dependent on several factors such as age, flow rate, intrapulmonary shunts due to pulmonary arterio-venous malformations (PAVMs) and pulmonary artery- and vein calibres. Even so, regressions of CFD and MRI results showed a correlation between simulated flow, and in-vivo flow measured in MRI of r=0.79, p=0.004 in paper I and r=0.94, p<0.001 in paper II.

Additionally, there was a learning curve in the development of methods to create anatomic models. Subjectively, we however found good visual agreement between all overlays of anatomies segmented from MRI, and coronal images obtained from fluoroscopic angiography, when available.

In this thesis, all flow distributions to the pulmonary arteries (PA) from the inferior vena cava (IVC) including blood from the liver and "hepatic factors", were calculated entirely based on CFD simulations. While this thesis did not provide

independent validation of the accuracy of these simulations, previously published work has demonstrated excellent agreement between CFD simulations of the IVC to PA flow in highly controlled in-vitro experiments with flow phantoms (83,84), using the same "established" CFD software we validated against in Paper II (108).

The results and conclusions presented in Paper III relied to a great extent on the assumption based on Ohms law, that the ratio of left to right pulmonary vein flow is a proxy for the ratio of right to left pulmonary vascular resistance. A confounder to these results is post-capillary contribution to pulmonary vein flow from other sources such as veno-venous collaterals (VVCs). An experienced paediatric radiologist who reviewed available radiological examinations found vessel pathways which suggested such contribution in two patients. While VVC flow in these vessels could not be quantified, we believe VVCs only had a minor contribution to the pulmonary vein flow as measured in the studied patients.

In Paper IV, due to the Covid pandemic some patients had a significantly longer time than the planned six months to the follow-up MRI. However, within the obtained follow-up times, the results did not suggest effects of longer or shorter follow-up times on the predictive capabilities of the proposed methods.

5.2 Interaction with wider society

At the time of publication of Paper II, Skåne University Hospital published a public press-release highlighting the potential benefits to patients of the presented research (Figure 5.2.1).

Figure 5.2.1. QR-code link: Press-release from Skåne University Hospital, Lund
Unique method provides faster postoperative recovery for children with congenital heart defects. Pressrelease © Region Skåne, link provided with permission from Region Skåne

When possible, families of patients participating in the prospective study in Paper IV received 3D-printed models of the Glenn- and TCPC vessels. Additionally, generic three-dimensional Augmented Reality (AR) heart models were produced with printouts handed out at many presentations and lectures (Figure 5.2.2).

1. Normal   2. HLHS   3. TCPC

Figure 5.2.2. Augmented Reality (AR) models of generic heart models with congenital defects
Scan the QR-codes with a smartphone or similar to download the AR-viewer application Vuforia View (PTC, Boston, MA, USA), which then reads these QR-codes to project AR-models on a flat surface.

6 Conclusions

This thesis concludes that rapid, predictive, pre-interventional computational fluid dynamics (CFD) simulations based on data from non-invasive magnetic resonance imaging (MRI) in patients with Fontan circulation are feasible and accurate, and that such simulations can routinely be performed within a day of MRI scanning, in contrast with up to a month which was previously reported. We believe this is the first time these objectives have been simultaneously achieved. Additionally, novel insights were presented related to hepatic-to-pulmonary flow and its effect on pulmonary flow and oxygen saturation at rest, potentially further contributing to the predictive capabilities of the proposed simulations.

The contributions of each paper to these conclusions are:

Paper I

Calculations of pulmonary blood flow in patients with Fontan circulation, incorporating effects of aortopulmonary collateral flow in simulated pulmonary vascular resistance, can predict pulmonary blood flow following invasive interventions.

Paper II

Computation times of the proposed predictive simulations can be as short as 3 minutes, compared with approximately 10-12 hours using more established and advanced CFD methods, with excellent agreement with the advanced method, and with measurements from MRI.

Paper III

There is a demonstrable and continuous relationship between hepatic-to-pulmonary blood flow, simulated pulmonary vascular resistance, pulmonary vein flow and oxygen saturation at rest. These relationships were maintained in a patient after an invasive intervention on the hepatic-to-pulmonary pathway, suggesting predictive capabilities of these findings.

Paper IV

Pre-surgical simulations of pulmonary flow based on MRI on the day before total cavo-pulmonary connection surgery can predict pulmonary flow, as measured with MRI approximately six months after surgery.

7 Future perspectives

Today, predictive simulations are only performed at few centres and for a limited range of congenital heart diseases where invasive interventions may be required. If more patients are to benefit from patient-specific, computationally optimized interventional designs, progress need to occur on several fronts:

1) Further reduction of lead time and cost of simulations.

2) Development of methods to simulate more types of invasive interventions.

3) Increased availability of simulations.

1) Further reduction of lead times and cost of simulation

Lead time can be reduced by improving efficiency in all steps of the simulation process (Figure 1.5.1 steps A-G). Advances in machine learning for MRI image processing and routine adoption of 4D-flow may shorten the time required for MRI scanning and result interpretation (steps A-B).

For patients with Fontan circulation, this thesis has provided progress on steps C-G (Figure 1.5.1) with reduction of simulation times from hours to just minutes with maintained accuracy (108), and with demonstrated lead times of less than a day of pre-interventional MRI compared to up to a month as previously reported (81). Further time-savings may be achieved mainly with faster segmentation and model preparation (Figure 1.5.1 C-D). Machine learning may be of help to automate segmentation (54). It will however remain essential that manual interventions of arbitrary complexity can easily be imposed on the model to represent interventional options.

An exciting area that may radically improve computation time is the advent of machine learning and deep neural networks to replicate the simulation process itself. A study by Liang *et al.* showed how machine learning was used as a surrogate to CFD, which provided hemodynamics in a human aorta in the time scale of a second (111).

2) Development of methods to simulate more types of invasive interventions

Whereas the focus of this thesis was simulations of relatively steady pulmonary flow in children with univentricular hearts, invasive interventions are commonly

performed on defects in the major arteries distal to the heart, on cardiac valves and on the myocardium within the heart itself. Thus, in congenital and adult heart disease there are many invasive interventions where patients may benefit from pre-interventional simulations.

Interventions on the great arteries, such as in patients with Tetralogy of Fallot, or with aortic coarctation are performed in an environment where flows are highly pulsatile. Physiologically, the elastic, or capacitive properties of the distal vasculature maintain pressure during highly pulsatile or even regurgitative inflows, which may occur for example in patients with Tetralogy of Fallot with significant pulmonary regurgitation. Therefore, pragmatic approaches need to be found to routinely calculate and include patient specific resistive and capacitive properties of the distal vascular bed. Preliminary testing suggested that this may be supported by the Lean CFD workflow. We previously showed that pulsatile simulations with six heartbeats could be performed in the time frame of one hour (108). With future gains in the computing power of standard computers, pulsatile simulations should therefore be achievable such that they can be used to inform medical decisions during ongoing invasive procedures.

Simulation of valvular interventions may require fluid-structure interaction (FSI) where the structural deformation of valves is simulated with one type of software for structural simulation, and flow is simulated in CFD software, with stepwise bidirectional updates of changed geometry and fluid load during the simulation (51). Routine simulation of patient-specific valve interventions will require rapid registration and segmentation of the valves, which then need to be co-registered with nearby regions of the intracardiac anatomy such that resulting flows and pressures are sufficiently accurate to inform and guide interventions.

Simulation of intracardiac flow has been shown to require high resolution images and may require automated registration to obtain patient-specific wall motion (112). Simulation of intracardiac interventions such as closure of atrial- and ventricular septal defects will additionally require biventricular simulation to capture inter-ventricular hemodynamic relations, as well as incorporation of a physiological model that can provide physiological boundary conditions of the peripheral circulatory system during the cardiac cycle, and in response to the intervention. Whereas co-simulation with simplified representations of the peripheral circulatory system has previously been utilized, physiological modulation of registered wall motion to represent variations in cardiac contractility may be an area for further exploration.

3) Increased availability of simulations

Currently, the tools and software involved in simulation are complex. Users must be proficient in many tools which require engineering experience and a significant investment in training.

Modern softwares that integrate several steps in the CFD simulation process can potentially reduce the workload for users who perform the simulations and may therefore speed up the learning curve for new users and increase adoption of predictive simulation at more centres. As an example, anatomic changes on the simulation model should be automatically propagated to all downstream steps in the simulation process so that it isn't done from scratch as a completely new simulation model for each surgical- or interventional option. The Lean CFD framework put forward in this thesis has many of these properties and provides a seamless user environment for segmentation, preparation, simulation, visualization, and iteration (Figure 1.5.1 C, D, E, F, G).

To increase availability of simulations it would also be beneficial if medical staff without previous engineering experience could perform simulations related to their areas of expertise.

In the short term, this may be partially achieved if engineers prepare patient-specific simulation models up to the point where only a few parameters related to the design of the intervention remain to be selected and evaluated. A surgeon or interventionist could then be provided with an intuitive graphical interface that allows adjustment of these parameters, start of computation and visualisation of results. Thus, variations of the intervention could be performed independently of the medical engineer who prepared the simulation.

It would be highly speculative to predict the advent of fully automated preparation of pre-interventional and predictive flow simulations. Given the heterogenous nature of congenital heart defects, the variety of potentially available interventions and the breadth of imaging modalities (and modality-specific imaging artefacts), it is likely that persons who are medically knowledgeable and proficient in the full simulation process will be required as part of the extended clinical team in the foreseeable future.

To conclude, I believe that integrated and pragmatic medical and engineering judgement will remain central to choose future simulation approaches that will provide just the right information to guide patient-specific invasive treatment.

8 References

1. Triedman JK, Newburger JW. Global birth prevalen. Circulation. 2016;

2. Liu Y, Chen S, Zühlke L, Black GC, Choy MK, Li N, et al. Global birth prevalence of congenital heart defects 1970-2017: Updated systematic review and meta-analysis of 260 studies. Int J Epidemiol. 2019;48(2):455–63.

3. Fahed AC, Gelb BD, Seidman JG, Seidman CE. Genetics of congenital heart disease: The glass half empty. Vol. 112, Circulation Research. Lippincott Williams and Wilkins; 2013. p. 707–20.

4. Sun RR, Liu M, Lu L, Zheng Y, Zhang P. Congenital Heart Disease: Causes, Diagnosis, Symptoms, and Treatments. Cell Biochem Biophys. 2015 Jul 1;72(3):857–60.

5. Triedman JK, Newburger JW. Trends in congenital heart disease. Circulation. 2016 Jun 21;133(25):2716–33.

6. de Zélicourt DA, Kurtcuoglu V. Patient-Specific Surgical Planning, Where Do We Stand? The Example of the Fontan Procedure. Ann Biomed Eng. 2016;44(1):174–86.

7. Slesnick TC, Yoganathan AP. Computational modeling of Fontan physiology: at the crossroads of pediatric cardiology and biomedical engineering. Int J Cardiovasc Imaging. 2014 Aug;30(6):1073–84.

8. Restrepo M, Colleen Crouch A, Haggerty CM, Rossignac J, Slesnick TC, Kanter KR, et al. Hemodynamic impact of superior vena cava placement in the y-graft fontan connection. Annals of Thoracic Surgery. 2016;101(1):183–9.

9. Cohn JN, Ferrari R, Sharpe N. Cardiac Remodeling-Concepts and Clinical Implications: A Consensus Paper From an International Forum on Cardiac Remodeling. 2000.

10. Boron W, Boulapep E. Medical Physiology. 2nd ed. Elsevier Saunders; 2012.

11. Carlsson M, Ugander M, Mosén H, Buhre T, Arheden H. Atrioventricular plane displacement is the major contributor to left ventricular pumping in healthy adults, athletes, and patients with dilated cardiomyopathy. Am J Physiol Heart Circ Physiol. 2007;292(10):1452–9.

12. Carlsson M, Ugander M, Heiberg E, Arheden H. The quantitative relationship between longitudinal and radial function in left,right, and total heart pumping in humans. Am J Physiol Heart Circ Physiol. 2007;293:636–44.

13. Carlsson M, Cain P, Holmqvist C, Stahlberg F, Lundback S, Arheden H. Total heart volume variation throughout the cardiac cycle in humans Study Population and Design. Am J Physiol Heart Circ Physiol. 2004;287:243–50.

14. Chung CS, Karamanoglu M, Kovács SJ. Duration of diastole and its phases as a function of heart rate during supine bicycle exercise. Am J Physiol Heart Circ Physiol. 2004;287:2003–8.

15. Gewillig M. The Fontan circulation. Heart. 2005 Jun 1 ;91(6):839–46.

16. Fontan F, Baudet E. Surgical repair of tricuspid atresia. Thorax. 1971 May 1;26(3):240–8.

17. Nayak S, Booker PD. The Fontan circulation. Continuing Education in Anaesthesia, Critical Care and Pain. 2008;8(1):26–30.

18. Giannico S, Trezzi M, Cantarutti N, Cafiero G, Ravà L, Adorisio R, et al. Late outcome of extracardiac Fontan patients: 32 years of follow-up. European Journal of Cardio-thoracic Surgery. 2022 Jul 1;62(1).

19. Mery CM, de León LE, Trujillo-Diaz D, Ocampo EC, Dickerson HA, Zhu H, et al. Contemporary Outcomes of the Fontan Operation: A Large Single-Institution Cohort. In: Annals of Thoracic Surgery. Elsevier USA; 2019. p. 1439–46.

20. Miyake M, Sakamoto J, Kondo H, Iwakura A, Doi H, Tamura T. Forty-year survival after Glenn procedure without Fontan procedure in patients with single ventricle. Eur J Cardiothorac Surg. 2022 Nov 2;

21. Dabal RJ, Kirklin JK, Kukreja M, Brown RN, Cleveland DC, Eddins MC, et al. The modern Fontan operation shows no increase in mortality out to 20 years: A new paradigm. Journal of Thoracic and Cardiovascular Surgery. 2014 Dec 1;148(6):2517-2524.e1.

22. Thornton SW, Meza JM, Prabhu NK, Kang L, Moya-Mendez ME, Parker LE, et al. Impact of Ventricular Dominance on Long-Term Fontan Outcomes: A 25-year Single-institution Study. Ann Thorac Surg. 2022 Dec 18;

23. Gewillig M, Goldberg DJ. Failure of the fontan circulation. Heart Fail Clin [Internet]. 2014;10(1):105–16.

24. Mazza GA, Gribaudo E, Agnoletti G. The pathophysiology and complications of fontan circulation. Acta Biomedica. 2021 Nov 1;92(5).

25. Henaine R, Vergnat M, Bacha EA, Baudet B, Lambert V, Belli E, et al. Effects of lack of pulsatility on pulmonary endothelial function in the Fontan circulation. Journal of Thoracic and Cardiovascular Surgery. 2013 Sep;146(3):522–9.

26. Alsaied T, Sleeper LA, Masci M, Ghelani SJ, Azcue N, Geva T, et al. Maldistribution of pulmonary blood flow in patients after the Fontan operation is associated with worse exercise capacity. Journal of Cardiovascular Magnetic Resonance. 2018;20(1):1–10.

27. Noonan P, Kudumula V, Anderson B, Ramchandani B, Miller P, Dhillon R, et al. Stenting of the left pulmonary artery after palliation of hypoplastic left heart syndrome. Catheterization and Cardiovascular Interventions [Internet]. 2016 Aug 24;88(2):225–32.

28. Schwartz MC, DeCampli WM, Pourmoghadam K, Iacono K, Nykanen D. Hybrid Pulmonary Artery Stenting at the Bidirectional Glenn or Fontan Operation in Patients With Single Ventricle Congenital Heart Disease. World J Pediatr Congenit Heart Surg. 2016 May;7(3):299–305.

29. Triedman JK, Bridges ND, Mayer JE, Lock JE. Prevalence and risk factors for aortopulmonary collateral vessels after Fontan and bidirectional Glenn procedures. J Am Coll Cardiol. 1993;22(1):207–15.

30. Kanter KR, Vincent RN, Raviele AA. Importance of acquired systemic-to-pulmonary collaterals in the Fontan operation. Annals of Thoracic Surgery. 1999;68(3):969–75.

31. Grosse-Wortmann L, Al-Otay A, Yoo SJ. Aortopulmonary collaterals after bidirectional cavopulmonary connection or fontan completion quantification with MRI. Circ Cardiovasc Imaging. 2009;2(3):219–25.

32. Latus H, Gummel K, Diederichs T, Bauer A, Rupp S, Kerst G, et al. Aortopulmonary collateral flow is related to pulmonary artery size and affects ventricular dimensions in patients after the Fontan procedure. PLoS One. 2013;8(11):1–9.

33. Bradley SM, Mccall MM, Sistino JJ, Radtke WAK. Aortopulmonary Collateral Flow in the Fontan Patient: Does It Matter? Ann Thorac Surg. 2001.

34. Kodama Y, Ishikawa Y, Kuraoka A, Nakamura M, Oda S, Nakano T, et al. Systemic-to-Pulmonary Collateral Flow Correlates with Clinical Condition Late After the Fontan Procedure. Pediatr Cardiol. 2020 Dec 1;41(8):1800–6.

35. Stern HJ. Aggressive Coiling of Aortopulmonary Collaterals in Single-Ventricle Patients Is Warranted. Pediatr Cardiol. 2010;31(4):449–53.

36. Powell AJ. Aortopulmonary collaterals in single-ventricle congenital heart disease how much do they count? Circ Cardiovasc Imaging. 2009;2(3):171–3.

37. Latus H, Kruppa P, Hofmann L, Reich B, Jux C, Apitz C, et al. Impact of aortopulmonary collateral flow and single ventricle morphology on longitudinal hemodynamics in Fontan patients: A serial CMR study. Int J Cardiol. 2020;311:28–34.

38. Poterucha JT, Johnson JN, Taggart NW, Cabalka AK, Hagler DJ, Driscoll DJ, et al. Embolization of Veno-venous Collaterals after the Fontan Operation Is Associated with Decreased Survival. Congenit Heart Dis. 2015;10(5):E230-6.

39. Kavarana MN, Jones JA, Stroud RE, Bradley SM, Ikonomidis JS, Mukherjee R. Pulmonary arteriovenous malformations after the superior cavopulmonary shunt: Mechanisms and clinical implications. Vol. 12, Expert Review of Cardiovascular Therapy. Expert Reviews Ltd.; 2014. p. 703–13.

40. Vettukattil JJ, Slavik Z, Lamb RK, Monro JL, Keeton BR, Tsang VT, et al. Intrapulmonary arteriovenous shunting may be a universal phenomenon in patients with the superior cavopulmonary anastomosis: A radionuclide study. Heart. 2000;83(4):425–8.

41. McElhinney DB, Kreutzer J, Lang P, Mayer JE, del Nido PJ, Lock JE. Incorporation of the hepatic veins into the cavopulmonary circulation in patients with heterotaxy and pulmonary arteriovenous malformations after a kawashima procedure. Annals of Thoracic Surgery. 2005 Nov;80(5):1597–603.

42. Duncan BW, Desai S. Pulmonary Arteriovenous Malformations after Cavopulmonary Anastomosis. Annals of Thoracic Surgery. 2003;76(5):1759–66.

43. Spearman AD, Gupta A, Pan AY, Gronseth EI, Thirugnanam K, Gudausky TM, et al. Hepatic Vein Blood Increases Lung Microvascular Angiogenesis and Endothelial Cell Survival — Toward an Understanding of

Univentricular Circulation. Semin Thorac Cardiovasc Surg. 2020;32(4):980–7.

44.   Srivastava D, Preminger T, Lock JE, Mandell V, Keane JF, Mayer JE, et al. Hepatic Venous Blood and the Development of Pulmonary Arteriovenous Malformations in Congenital Heart Disease. Circulation. 1995 Sep;92(5):1217–22.

45.   Hoffman JIE. Normal and abnormal pulmonary arteriovenous shunting: Occurrence and mechanisms. Vol. 23, Cardiology in the Young. 2013. p. 629–41.

46.   Boscolo E, Wary KK, Spearman AD. Hepatic factor may not originate from hepatocytes. Front Cardiovasc Med. 2022.

47.   Dori Y, Sathanandam S, Glatz AC, Gillespie MJ, Rome JJ. Catheter approach to redirect hepatic venous return for treatment of unilateral pulmonary arteriovenous malformations after fontan. Catheter Cardiovasc Interv. 2013;00(November 2013):86–93.

48.   Sjöberg P, Hedström E, Fricke K, Frieberg P, Weismann CG, Liuba P, et al. Comparison of 2D and 4D Flow MRI in Neonates Without General Anesthesia. Journal of Magnetic Resonance Imaging. 2022;1–12.

49.   Azarine A, Garçon P, Stansal A, Canepa N, Angelopoulos G, Silvera S, et al. Four-dimensional Flow MRI: Principles and Cardiovascular Applications. Vol. 39, Radiographics : a review publication of the Radiological Society of North America, Inc. NLM (Medline); 2019. p. 632–48.

50.   Versteeg HK, Malalasekera W. An Introduction to Computational Fluid Dynamics. 2nd ed. Pearson Prentice Hall; 2007.

51.   Rego B v., Khalighi AH, Drach A, Lai EK, Pouch AM, Gorman RC, et al. A noninvasive method for the determination of in vivo mitral valve leaflet strains. Int J Numer Method Biomed Eng. 2018 Dec;34(12):e3142.

52.   Kamio T, Suzuki M, Asaumi R, Kawai T. DICOM segmentation and STL creation for 3D printing: a process and software package comparison for osseous anatomy. 3D Print Med. 2020 Dec;6(1).

53.   Ganapathy A, Chen D, Elumalai A, Albers B, Tappa K, Jammalamadaka U, et al. Guide for starting or optimizing a 3D printing clinical service. Methods. 2022 Oct 1;206:41–52.

54.   Montalt-Tordera J, Pajaziti E, Jones R, Sauvage E, Puranik R, Singh AAV, et al. Automatic segmentation of the great arteries for computational

hemodynamic assessment. Journal of Cardiovascular Magnetic Resonance. 2022 Dec 1;24(1).

55. Ryd D, Nilsson A, Heiberg E, Hedström E. Automatic Segmentation of the Fetus in 3D Magnetic Resonance Images Using Deep Learning: Accurate and Fast Fetal Volume Quantification for Clinical Use. Pediatr Cardiol. 2022;

56. Wei ZA, Huddleston C, Trusty PM, Singh-Gryzbon S, Fogel MA, Veneziani A, et al. Analysis of Inlet Velocity Profiles in Numerical Assessment of Fontan Hemodynamics. Ann Biomed Eng. 2019 Nov 24;47(11):2258–70.

57. Wei Z, Singh-Gryzbon S, Trusty PM, Huddleston C, Zhang Y, Fogel MA, et al. Non-Newtonian Effects on Patient-Specific Modeling of Fontan Hemodynamics. Ann Biomed Eng. 2020;48(8):2204–17.

58. Frieberg P, Sjöberg P, Revstedt J, Heiberg E, Liuba P, Carlsson M. Simulation of aortopulmonary collateral flow in Fontan patients for use in prediction of interventional outcomes. Clin Physiol Funct Imaging. 2018;38(4).

59. Somnath R, De A, Balaras E, editors. Immersed Boundary Method, Development And Applications. Springer; 2020.

60. Mittal R, Iaccarino G. IMMERSED BOUNDARY METHODS. Annu Rev Fluid Mech. 2005 Jan;37(1):239–61.

61. Zélicourt D de, Ge L, Wang C, Sotiropoulos F, Gilmanov A, Yoganathan A. Flow simulations in arbitrarily complex cardiovascular anatomies - An unstructured Cartesian grid approach. Comput Fluids. 2009;38(9):1749–62.

62. Ahmed Y, Tossas-Betancourt C, van Bakel PAJ, Primeaux JM, Weadock WJ, Lu JC, et al. Interventional Planning for Endovascular Revision of a Lateral Tunnel Fontan: A Patient-Specific Computational Analysis. Front Physiol. 2021;12(August):1–11.

63. Corsini C, Baker C, Kung E, Schievano S, Arbia G, Baretta A, et al. An integrated approach to patient-specific predictive modeling for single ventricle heart palliation. Comput Methods Biomech Biomed Engin. 2014 Oct 26;17(14):1572–89.

64. Mirabella L, Haggerty CM, Passerini T, Piccinelli M, Powell AJ, del Nido PJ, et al. Treatment planning for a TCPC test case: A numerical investigation under rigid and moving wall assumptions. Int J Numer Method Biomed Eng. 2013 Feb;29(2):197–216.

65. Tang E, Wei Z, Fogel MA, Veneziani A, Yoganathan AP. Fluid-structure interaction simulation of an intra-atrial fontan connection. Biology (Basel). 2020 Dec 1;9(12):1–20.

66. McHugo S, Nolke L, Delassus P, MacCarthy E, Morris L, McMahon CJ. An in-vitro evaluation of the flow haemodynamic performance of Gore-Tex extracardiac conduits for univentricular circulation. J Cardiothorac Surg. 2020 Sep 2;15(1).

67. Haggerty CM, Kanter KR, Restrepo M, de Zélicourt D a, Parks WJ, Rossignac J, et al. Simulating hemodynamics of the Fontan Y-graft based on patient-specific in vivo connections. J Thorac Cardiovasc Surg. 2013 Mar;145(3):663–70.

68. Yang W, Chan FP, Reddy VM, Marsden AL, Feinstein J a. Flow simulations and validation for the first cohort of patients undergoing the Y-graft Fontan procedure. J Thorac Cardiovasc Surg [Internet]. 2014 Sep 21;149(1):247–55.

69. Nader E, Skinner S, Romana M, Fort R, Lemonne N, Guillot N, et al. Blood rheology: Key parameters, impact on blood flow, role in sickle cell disease and effects of exercise. Vol. 10, Frontiers in Physiology. Frontiers Media S.A.; 2019.

70. Chien S, Usami S, Dellenback RJ, Gregersen MI. Blood Viscosity: Influence of Erythrocyte Aggregation. Vol. 157, New Series. 1967.

71. Cheng AL, Takao CM, Wenby RB, Meiselman HJ, Wood JC, Detterich JA. Elevated Low-Shear Blood Viscosity is Associated with Decreased Pulmonary Blood Flow in Children with Univentricular Heart Defects. Pediatr Cardiol. 2016 Apr 1;37(4):789–801.

72. Bossers SSM, Cibis M, Gijsen FJ, Schokking M, Strengers JLM, Verhaart RF, et al. Computational fluid dynamics in Fontan patients to evaluate power loss during simulated exercise. Heart. 2014 May;100(9):696–701.

73. Yang W, Feinstein J a., Marsden AL. Constrained optimization of an idealized Y-shaped baffle for the Fontan surgery at rest and exercise. Comput Methods Appl Mech Eng. 2010 Jul;199(33–36):2135–49.

74. Baretta A, Corsini C, Yang W, Vignon-Clementel IE, Marsden AL, Feinstein JA, et al. Virtual surgeries in patients with congenital heart disease: A multi-scale modelling test case. Philosophical Transactions of the Royal Society A: Mathematical, Physical and Engineering Sciences. 2011;

75. Bove EL, de Leval MR, Migliavacca F, Guadagni G, Dubini G. Computational fluid dynamics in the evaluation of hemodynamic

performance of cavopulmonary connections after the norwood procedure for hypoplastic left heart syndrome. J Thorac Cardiovasc Surg. 2003 Oct; 126(4):1040–7.

76. Moon JY, Suh DC, Lee YS, Kim YW, Lee JS. Considerations of blood properties, outlet boundary conditions and energy loss approaches in computational fluid dynamics modeling. Neurointervention. 2014 Feb;9(1):1–8.

77. Menon PG, Yoshida M, Pekkan K. Presurgical Evaluation of Fontan Connection Options for Patients With Apicocaval Juxtaposition Using Computational Fluid Dynamics. Artif Organs. 2013;37(1).

78. Khiabani RH, Whitehead KK, Han D, Restrepo M, Tang E, Bethel J, et al. Exercise capacity in single-ventricle patients after Fontan correlates with haemodynamic energy loss in TCPC. Heart. 2015;101(2).

79. Rijnberg FM, van 't Hul LC, Hazekamp MG, van den Boogaard PJ, Juffermans JF, Lamb HJ, et al. Haemodynamic performance of 16–20-mm extracardiac Goretex conduits in adolescent Fontan patients at rest and during simulated exercise. European Journal of Cardio-Thoracic Surgery. 2022 Dec 2;63(1).

80. Marsden AL, Vignon-Clementel IE, Chan FP, Feinstein JA, Taylor CA. Effects of exercise and respiration on hemodynamic efficiency in CFD simulations of the total cavopulmonary connection. Ann Biomed Eng. 2007;35(2):250–63.

81. Trusty PM, Slesnick TC, Wei ZA, Rossignac J, Kanter KR, Fogel MA, et al. Fontan surgical planning: Previous accomplishments, current challenges, and future directions. Vol. 11, Journal of Cardiovascular Translational Research. Springer New York LLC; 2018. p. 133–44.

82. Wei ZA, Trusty PM, Tree M, Haggerty CM, Tang E, Fogel M, et al. Can time-averaged flow boundary conditions be used to meet the clinical timeline for Fontan surgical planning? J Biomech. 2017;50:172–9.

83. Liu X, Aslan S, Kim B, Warburton L, Jackson D, Muhuri A, et al. Computational Fontan Analysis: Preserving Accuracy While Expediting Workflow. World J Pediatr Congenit Heart Surg. 2022 May;13(3):293–301.

84. Rasooli R, Kose B, Samaneh Lashkarinia S, Sasmazel A, Pekkan K. In vitro measurement of hepatic flow distribution in Fontan vascular conduits: Towards rapid validation techniques. J Biomech. 2022;137(April):111092.

85. Wei ZA, Fogel MA. Engineering Perspective on Cardiovascular Simulations of Fontan Hemodynamics: Where Do We Stand with a Look Towards Clinical Application. Cardiovasc Eng Technol. 2021 Dec 1;12(6):618–30.

86. Sjöberg P, Heiberg E, Wingren P, Ramgren Johansson J, Malm T, Arheden H, et al. Decreased Diastolic Ventricular Kinetic Energy in Young Patients with Fontan Circulation Demonstrated by Four-Dimensional Cardiac Magnetic Resonance Imaging. Pediatr Cardiol. 2017 Apr 1;38(4):669–80.

87. Töger J, Bidhult S, Revstedt J, Carlsson M, Heiberg E. Independent validation of four-dimensional flow MR velocities and vortex ring volume using particle imaging velocimetry and planar laser-Induced fluorescence. Magn Reson Med. 2016;75(3):1064–75.

88. Töger J, Kanski M, Carlsson M, Kovács SJ, Söderlind G, Arheden H, et al. Vortex Ring Formation in the Left Ventricle of the Heart: Analysis by 4D Flow MRI and Lagrangian Coherent Structures. Ann Biomed Eng. 2012;40(12):1–11.

89. Carlsson M, Töger J, Kanski M, Bloch KM, Ståhlberg F, Heiberg E, et al. Quantification and visualization of cardiovascular 4D velocity mapping accelerated with parallel imaging or k-t BLAST: head to head comparison and validation at 1.5 T and 3 T. J Cardiovasc Magn Reson. 2011 Oct 4;13(1):55.

90. Liefke J, Heijl C, Steding-Ehrenborg K, Morsing E, Arheden H, Ley D, et al. Fetal growth restriction followed by very preterm birth is associated with smaller kidneys but preserved kidney function in adolescence. Pediatric Nephrology. 2022;

91. Schulz-Menger J, Bluemke DA, Bremerich J, Flamm SD, Fogel MA, Friedrich MG, et al. Standardized image interpretation and post processing in cardiovascular magnetic resonance: Society for Cardiovascular Magnetic Resonance (SCMR) Board of Trustees Task Force on Standardized Post Processing. Journal of Cardiovascular Magnetic Resonance. 2013;15(1).

92. Heiberg E, Sjögren J, Ugander M, Carlsson M, Engblom H, Arheden H. Design and validation of Segment-freely available software for cardiovascular image analysis. BMC Med Imaging. 2010.

93. Sun Q, Liu J, Qian Y, Hong H, Liu J. Using of porous portion to simulate pulmonary resistance in the computational fluid dynamic models of Fontan connection. Proceedings of the Annual International Conference of the IEEE Engineering in Medicine and Biology Society, EMBS. 2013 Jan;2013:481–4.

94. Hameed M, Prather R, Divo E, Kassab A, Nykanen D, Farias M, et al. Computational fluid dynamics investigation of the novel hybrid comprehensive stage II operation. JTCVS Open. 2021 Sep 1;7:308–23.

95. Ni MW, Prather RO, Rodriguez G, Quinn R, Divo E, Fogel M, et al. Computational Investigation of a Self-Powered Fontan Circulation. Cardiovasc Eng Technol. 2018 Jun 1;9(2):202–16.

96. Hull JE, Balakin B v., Kellerman BM, Wrolstad DK. Computational fluid dynamic evaluation of the side-to-side anastomosis for arteriovenous fistula. J Vasc Surg. 2013;58(1).

97. Febina J, Sikkandar MY, Sudharsan NM. Wall Shear Stress Estimation of Thoracic Aortic Aneurysm Using Computational Fluid Dynamics. Comput Math Methods Med. 2018;2018.

98. Aristokleous N, Seimenis I, Georgiou GC, Papaharilaou Y, Brott BC, Nicolaides A, et al. Impact of head rotation on the individualized common carotid flow and carotid bifurcation hemodynamics. IEEE J Biomed Health Inform. 2014;18(3):783–9.

99. Aristokleous N, Houston JG, Browne LD, Broderick SP, Kokkalis E, Gandy SJ, et al. Morphological and hemodynamical alterations in brachial artery and cephalic vein. An image-based study for preoperative assessment for vascular access creation. Int J Numer Method Biomed Eng. 2018;34(11):e3136.

100. Khiabani RH, Restrepo M, Tang E, de Zélicourt D, Sotiropoulos F, Fogel M, et al. Effect of flow pulsatility on modeling the hemodynamics in the total cavopulmonary connection. J Biomech. 2012 Sep;45(14):2376–81.

101. Malek AM. Hemodynamic Shear Stress and Its Role in Atherosclerosis. JAMA. 1999 Dec 1;282(21):2035.

102. Sengupta D, Kahn AM, Burns JC, Sankaran S, Shadden SC, Marsden AL. Image-based modeling of hemodynamics in coronary artery aneurysms caused by Kawasaki disease. Biomech Model Mechanobiol. 2012 Jul;11(6):915–32.

103. Whitehead KK, Harris MA, Glatz AC, Gillespie MJ, DiMaria M v., Harrison NE, et al. Status of Systemic to Pulmonary Arterial Collateral Flow After the Fontan Procedure. American Journal of Cardiology. 2015;115(12):1739–45.

104. Pennati G, Migliavacca F, Dubini G, Pietrabissa R, Fumero R, de Leval MR. Use of mathematical model to predict hemodynamics in cavopulmonary anastomosis with persistent forward flow. Journal of Surgical Research. 2000;89(1):43–52.

105. Gewillig M, Brown SC. The Fontan circulation after 45 years: update in physiology. Heart. 2016 Jul 15;102(14):1081–6.

106. Wang C, Pekkan K, de Zélicourt D, Horner M, Parihar A, Kulkarni A, et al. Progress in the CFD modeling of flow instabilities in anatomical total cavopulmonary connections. Ann Biomed Eng. 2007;35(11):1840–56.

107. Haggerty CM, de Zélicourt D a, Restrepo M, Rossignac J, Spray TL, Kanter KR, et al. Comparing Pre- and Post-operative Fontan Hemodynamic Simulations: Implications for the Reliability of Surgical Planning. Ann Biomed Eng. 2012 Dec 10;40(12):2639–51.

108. Frieberg P, Aristokleous N, Sjöberg P, Töger J, Liuba P, Carlsson M. Computational Fluid Dynamics Support for Fontan Planning in Minutes, Not Hours: The Next Step in Clinical Pre-Interventional Simulations. J Cardiovasc Transl Res. 2021;

109. Wieslander B, Ramos JG, Ax M, Petersson J, Ugander M. Supine, prone, right and left gravitational effects on human pulmonary circulation. Journal of Cardiovascular Magnetic Resonance. 2019;21(1):1–15.

110. Trusty PM, Wei ZA, Slesnick TC, Kanter KR, Spray TL, Fogel MA, et al. The first cohort of prospective Fontan surgical planning patients with follow-up data: How accurate is surgical planning? Journal of Thoracic and Cardiovascular Surgery. 2019;157(3):1146–55.

111. Liang L, Mao W, Sun W. A feasibility study of deep learning for predicting hemodynamics of human thoracic aorta. J Biomech. 2020 Jan 23;99.

112. Lantz J, Henriksson L, Persson A, Karlsson M, Ebbers T. Patient-Specific Simulation of Cardiac Blood Flow from High-Resolution Computed Tomography. J Biomech Eng. 2016 Dec 1;138(12).

FACULTY OF
MEDICINE